SCATTERING OF AN ENTROPY DISTURBANCE INTO SOUND BY A LINEAR CASCADE OF TURBINE STATOR BLADES

BY

ASHISH MISHRA

THESIS

Submitted in partial fulfillment of the requirements
for the degree of Master of Science in Aerospace Engineering
in the Graduate College of the
University of Illinois at Urbana-Champaign, 2011

Urbana, Illinois

Advisor:

Professor Daniel J. Bodony

Abstract

It is known that modern turbofan engines produce more noise from their exhaust than can be accounted for by jet noise alone. Part of the extra noise coming from the exhaust of the engine is associated with the combustor. Apart from direct combustion noise, the combustor is known to have an indirect source of noise in the form of the interaction of convecting entropy disturbances with the turbine blades. This indirect noise generation is due to the (i) acceleration of the convected disturbance by the mean flow and (ii) satisfaction of the wall-boundary condition on the turbine blades. The indirect combustion noise is known to be present in modern gas turbine engines but its specific details are not known, including its overall contribution to the acoustic signature of the engine and its influence on the combustor. The present work focuses on carrying out direct numerical simulations for various cases of interaction between the entropy disturbance and turbine stator vane. Combustor-produced entropy disturbances have been simulated both in the form of a plane wave and localized high frequency pulse. DNS results for the interaction of an entropy disturbance with turbine stator vanes are presented and the resulting pressure disturbance field is analyzed. The DNS results are used to verify the analytical predictions of actuator disk theory.

The actuator disk theory (ADT) ignores the geometric details of a blade under the assumption that wavelengths of all the disturbances are much longer than the chord length of the blade and replaces it with a discontinuity at position x_0, referred in this thesis as the origin of the noise source. Actuator disk theory only uses the inlet and outlet flow Mach number and flow angle to compute the pressure disturbance field caused by an input entropy disturbance. One feature of this two-dimensional theory is the presence of evanescent modes below the cut-off wavelength, which decay in amplitude away from the blade, and also the independence of cut-on modes with the

upstream and downstream distance from the blade. It is observed that for a low-frequency planar input entropy wave the decay rates for modes of larger wavelengths are very well predicted but as wavelengths goes smaller and smaller, matching between ADT predictions and DNS results worsens. The measured decay rate for smallest wavelengths is invariably lower than the ADT predictions. Comparisons between cut-on modes have been performed using the plane-mode values of pressure disturbance spectrum. It is observed that ADT predictions work reasonably well for low-frequency waves both upstream and downstream of the blade. The location of x_0 has been computed using DNS results and it is found that ADT predictions are reasonable if we keep leading edge of the blade as origin of noise source for upstream traveling waves whereas trailing edge is better suited location for x_0 when it comes to downstream traveling waves. At higher frequencies the accuracy of ADT predictions suffers.

To my father.

Acknowledgments

To begin with, I would like to express my gratitude to my advisor, Dr. Bodony, who lead me through this journey not only as a mentor but also as a friend. I have had many fruitful and insightful discussions with him which lead me to have a better understanding of not only the work at hand but also of fluid mechanics as a whole. His exemplary dedication for his work is inspiring and has taught me to be focused on the work at hand.

Discussions with Mahesh Natarajan, Qi Zhang, Nishan Jain, Mahesh Manchakattil, Christopher Ostoich, Jeonglae Kim, Revathi Nathan and everyone else in my research group also greatly enhanced my understandings of basic fundamentals of fluid mechanics and in general taught me about research and the expression of ideas.

This work was supported by NASA, through the subsonic fixed wing NRA program, project NNX07AB90A. Dr. Lennart Hultgren was the technical monitor. Computational resources from the Turing cluster, operated by the Computational Science and Engineering Department, University of Illinois at Urbana-Champaign, are greatly acknowledged.

Finally, from the bottom of my heart I would like to express sincere gratitude to my parents, sister, and brother for their help and guidance. In particular, I would like to express gratitude to my father who has shown me the path of self dependence, honesty and truth and instilled these virtues in me by his exemplary high standards.

Table of Contents

Nomenclature . . . . . **vii**

List of Tables . . . . . **x**

List of Figures . . . . . **xi**

Chapter 1 Introduction **1**
1.1 Literature Review 1
1.2 The structure of the thesis 6

Chapter 2 Actuator disk theory **8**
2.1 Characteristic of the actuator disk 10
2.2 Analytical details 12
2.3 Reproduction of results of ADT 17
2.3.1 Isolated blade row: stator vane 17
2.4 Figures for chapter 2 19

Chapter 3 Direct numerical simulation of entropy disturbance scattering into sound **21**
3.1 Computational details 21
3.2 Numerical method 22
3.3 Grid converged mean flow 23
3.4 Plane-wave entropic disturbance 24
3.4.1 Comparison of DNS results with ADT 25
3.5 Figures of chapter 3 30

Chapter 4 Direct numerical simulation of localized entropy disturbance **41**
4.1 Comparison of DNS results with ADT 43
4.2 Comparison with low frequency planar wave 46
4.3 Figures of chapter 4 49

Chapter 5 Conclusions and future work **67**
5.1 Summary 67
5.2 Conclusions 67
5.3 Future work 69

References **70**

Nomenclature

List of Abbreviations

NASA	National Aeronautics and Space Administration
ADT	Actuator disk theory
EWG	Entropy Wave Generator
CERTS	Combustor Exit Radial Temperature Simulator
DNS	Direct Numerical Simulation
RK4	fourth order Runge-Kutta
FFT	fast Fourier transform
pw	Plane wave
hs	Hot spot

List of Symbols

Greek Symbols

α, β	Coefficients in the left-hand-side of the Padé schemes
γ	Ratio of specific heats at constant pressure and volume
θ'	Fluctuation in the flow angle
θ	Mean flow angle
ρ	Mean flow density

ξ'	Vorticity fluctuation
ξ	Amplitude of vorticity wave
θ	Mean flow angle
ν_s	Angle at which normal to the entropy wave is inclined with respect to the $x-$ axis
ω	Temporal frequency of entropy wave (radian)
σ	Amplitude of the entropy wave
ν_ξ	Angle at which normal to the vorticity wave is inclined with respect to the $x-$ axis
θ'_ξ	Flow angle fluctuation due to vorticity wave
$\alpha^\pm$	Argument of of downstream and upstream moving acoustic wave
θ'_a	Flow angle fluctuation due to acoustic wave
ν	Angle at which normal to the acoustic wave is inclined with respect to the $x-$ axis
β	ratio of static temperature and total temperature for an isentropic process

Roman Symbols

s'	Entropy fluctuations
c_p	Specific heat capacity at constant pressure
p'	Pressure fluctuations
p	Mean pressure
w'	Velocity fluctuation
W	Mean flow velocity
a	Speed of sound
M	Mean Mach number
k_s	Scalar wave number for entropy wave
u'_s	Axial velocity fluctuation due to entropy fluctuation
v'_s	Azimuthal velocity fluctuation due to entropy fluctuation
p'_s	Pressure fluctuation due to entropy fluctuation
k_ξ	Scalar wave number for vorticity wave
w'_ξ	Velocity fluctuation due to vorticity wave

p^{ν}	Amplitude of pressure wave
k_x	Axial wavenumber for pressure wave
k_y	Azimuthal wavenumber for pressure wave
$p^{\nu,\pm}$	Amplitude of downstream and upstream traveling pressure wave
k_x^1	Real part of complex valued axial wavenumber for pressure wave
k_x^2	Imaginary part of complex valued axial wavenumber for pressure wave
w'_a	Velocity fluctuation due to acoustic wave
B_I	Input coefficient matrix
V_I	Input vector
B_O	Output coefficient matrix
V_O	Output vector
f	Temporal frequency
Y	Azimuthal wavelength

Subscripts, Superscripts and Accents

$(\cdot)_\infty$	Freestream variable
$(\cdot)_1$	Upstream station
$(\cdot)_2$	Downstream station
$(\cdot)_s$	Variables corresponding to entropy wave
$(\cdot)_\xi$	Variables corresponding to vorticity wave
$(\cdot)_a$	Acoustic variables
$\hat{(\cdot)}$	Fourier transformed variable
$(\cdot)'$	Fluctuation in a quantity
$(\cdot)^+$	Downstream traveling pressure wave
$(\cdot)^-$	Upstream traveling pressure wave
$\|\|(\cdot)\|\|$	Modulus or Magnitude of the variables

List of Tables

3.1 Freestream flow conditions: CERTS turbine 22
3.2 Freestream flow conditions: modern turbine 22
3.3 Parameters for direct simulation: Entropy disturbance as a plane-wave 24
3.4 Upstream and downstream flow parameters for ADT 26
3.5 Comparison of upstream plane-mode values 27
3.6 Comparison of downstream plane-mode values 28

4.1 Parameters for direct simulation: Localized entropy pulse. 42
4.2 Upstream and downstream flow parameters for ADT 44
4.3 Comparison of upstream plane-mode values 46
4.4 Comparison of downstream plane-mode values 46
4.5 Comparison of plane-mode values 48

List of Figures

2.1 Reproduction of downstream actuator disk results presented by Cumpsty and Marble [22]. $M_1 = 0.20$, $\theta_1 = 0^o$, $M_2 = 0.95$, $\theta_2 = 70.4^o$. Legend: ● original result for right moving pressure wave; ○ original result for left moving pressure wave; — reproduced result for right moving pressure wave; – – – reproduced result for left moving pressure wave. 19

2.2 Reproduction of upstream actuator disk results presented by Cumpsty and Marble [22]. $M_1 = 0.20$, $\theta_1 = 0^o$, $M_2 = 0.95$, $\theta_2 = 70.4^o$. Legend: ● original result for right moving pressure wave; □ original result for left moving pressure wave; — reproduced result for right moving pressure wave; – – – reproduced result for left moving pressure wave. 20

3.1 Computational domain and boundary conditions. 30

3.2 Contours of density ρ_0 representing the mean flow over stator vane. Square boxes represent probes near leading and trailing edges. Contour range from $0.5\rho_\infty$ to $\rho_i nfty$ 31

3.3 Grid converged mean flow: comparison between pressure fluctuations for grids with 0.3 M and 1.2 M grid points at upstream and downstream probe stations. Legend: –– 0.3 M and — 1.2 M. 32

3.4 Four consecutive instantaneous views of the density disturbance (solid lines) and pressure disturbance (contours) corresponding to test case pw1. Time increases from left to right. Density contour lines of $|\rho'| \leq 1.0 \times 10^{-3}\rho_\infty$ and pressure contours of $|P'| \leq 1.5 \times 10^{-3}P_\infty$ are shown. 33

3.5 Probe stations for evaluation of DNS results. 34

3.6 3-dimensional representation of azimuthal and temporal variation of pressure fluctuations at various upstream probe stations.The z-label is $|p'/\gamma p|$ 35

3.7 3-dimensional representation of azimuthal and temporal variation of pressure fluctuations at various downstream probe stations. The z-label is $|p'/\gamma p|$ 36

3.8 Comparison between pressure fluctuation magnitude of ADT and DNS results at upstream probe stations for incoming plane waves of 1000 Hz, 700 Hz, 400 Hz and non-planar wave of 1100 Hz. Legend: — ADT prediction for right moving wave, 400 Hz; ▲ DNS result for right moving wave, 400 Hz; – – – ADT prediction for left moving wave, 400 Hz; △ DNS result for left moving wave, 400 Hz; — ADT prediction for right moving wave, 700 Hz; ■ DNS result for right moving wave, 700 Hz; – – – ADT prediction for left moving wave, 700 Hz; □ DNS result for left moving wave, 700 Hz; — ADT prediction for right moving wave, 1000 Hz; ♦ DNS result for right moving wave, 1000 Hz; – – – ADT prediction for left moving wave, 1000 Hz; ◊ DNS result for left moving wave, 1000 Hz; — ADT prediction for right moving wave, 1100 Hz; ● DNS result for right moving wave, 1100 Hz; – – – ADT prediction for left moving wave, 1100 Hz; ○ DNS result for left moving wave, 1100 Hz. 37

3.9 Comparison between pressure fluctuation magnitude of ADT and DNS results at downstream probe stations for incoming plane waves of 1000 Hz, 700 Hz, 400 Hz and non-planar wave of 1100 Hz. Legend: — ADT prediction for right moving wave, 400 Hz; ▲ DNS result for right moving wave, 400 Hz; – – – ADT prediction for left moving wave, 400 Hz; △ DNS result for left moving wave, 400 Hz; — ADT prediction for right moving wave, 700 Hz; ■ DNS result for right moving wave, 700 Hz; – – – ADT prediction for left moving wave, 700 Hz; □ DNS result for left moving wave, 700 Hz; — ADT prediction for right moving wave, 1000 Hz; ♦ DNS result for right moving wave, 1000 Hz; – – – ADT prediction for left moving wave, 1000 Hz; ◊ DNS result for left moving wave, 1000 Hz; — ADT prediction for right moving wave, 1100 Hz; ● DNS result for right moving wave, 1100 Hz; – – – ADT prediction for left moving wave, 1100 Hz; ○ DNS result for left moving wave, 1100 Hz. Inset figures show the plane azimuthal mode corresponding to different cases. . 38

3.10 Comparison of axial decay rate between the DNS results and ADT predictions. Legend: ▲ right moving wave, 400 Hz; ■ right moving wave, 700 Hz; ♦ right moving wave, 1000 Hz; ● right moving wave, 1100 Hz; 39

3.11 Location of perceived noise source in DNS results and its relative distance from leading and trailing edges for upstream and downstream waves. $x_0 = x_L E$ for upstream and $x_0 = x_T E$ for downstream. Legend: ▲ right moving wave, 400 Hz; ■ right moving wave, 700 Hz; ♦ right moving wave, 1000 Hz; ● right moving wave, 1100 Hz; 40

4.1 Computational domain and boundary conditions. 49

4.2 Four consecutive instantaneous views of the density disturbance (solid lines) and pressure disturbance (contours) corresponding to test case hs1. Time increases from left to right. Density contour lines of $|\rho'| \leq 1.0 \times 10^{-4}\rho_\infty$ and pressure contours of $|P'| \leq 1.0 \times 10^{-6}P_\infty$ are shown. 50

4.3 Four consecutive instantaneous views of the density disturbance (solid lines) and pressure disturbance (contours) corresponding to test case hs4. Time increases from left to right. Density contour lines of $|\rho'| \leq 1.0 \times 10^{-4}\rho_\infty$ and pressure contours of $|P'| \leq 1.0 \times 10^{-6}P_\infty$ are shown. 51

4.4 Linear dependence of pressure fluctuation on amplitude, A of incoming entropy pulse. Legend: ● hs1; ♦ hs6; ▲ hs7. 52

4.5 Variation of pressure disturbance with time at the upstream probe station near the leading edge shown in figure 3.2. 53
4.6 Variation of pressure disturbance with time at the downstream probe station near the trailing edge shown in figure 3.2. 54
4.7 Linear dependence of pressure fluctuation on initial vertical location, y_0 of incoming entropy pulse. Legend: ■ hs1; ▲ hs2. ○ hs3; ♦ hs4; ● hs5. 55
4.8 Comparison between pressure fluctuation magnitude of ADT and DNS results at the first upstream probe station. Legend: — ADT prediction for right moving wave; ● DNS result for right moving wave; – – – ADT prediction for left moving wave; ○ DNS result for left moving wave. Inset figure shows the plane azimuthal mode. . 56
4.9 Comparison between pressure fluctuation magnitude of ADT and DNS results at the downstream probe stations. Legend: — ADT prediction for right moving wave; ● DNS result for right moving wave; – – – ADT prediction for left moving wave; ○ DNS result for left moving wave. Inset figures show the plane azimuthal mode corresponding to different cases. 57
4.10 Comparison of axial decay rate between the DNS results and ADT predictions. Legend: ● right moving wave, 5088 Hz; 58
4.11 Location of perceived noise source in DNS results and its relative distance from leading and trailing edges for upstream and downstream waves. $x_0 = x_L E$ for upstream and $x_0 = x_T E$ for downstream. Legend: ● right moving wave, 5088 Hz; 59
4.12 Four consecutive instantaneous views of the density disturbance (solid lines) and pressure disturbance (contours) corresponding to plane wave of 1000 Hz. Time increases from left to right. Density contour lines of $|\rho'| \leq 1.0 \times 10^{-3}\rho_\infty$ and pressure contours of $|P'| \leq 1.0 \times 10^{-3}p_\infty$ are shown. 60
4.13 3-dimensional representation of azimuthal and temporal variation of pressure fluctuations at various upstream probe stations. The z-label is$|p'/\gamma p|$ 61
4.14 3-dimensional representation of azimuthal and temporal variation of pressure fluctuations at various downstream probe stations. The z-label is$|p'/\gamma p|$ 62
4.15 Comparison between pressure fluctuation magnitude of ADT and DNS results at the downstream probe stations. Legend: — ADT prediction for right moving wave; ● DNS result for right moving wave; – – – ADT prediction for left moving wave; ○ DNS result for left moving wave. Inset figures show the plane azimuthal mode corresponding to different cases. 63
4.16 Comparison between pressure fluctuation magnitude of ADT and DNS results at the downstream probe stations. Legend: — ADT prediction for right moving wave; ● DNS result for right moving wave; – – – ADT prediction for left moving wave; ○ DNS result for left moving wave. Inset figures show the plane azimuthal mode corresponding to different cases. 64
4.17 Comparison of axial decay rate between the DNS results and ADT predictions. Legend: ● right moving wave, 1000 Hz; 65
4.18 Location of perceived noise source in DNS results and its relative distance from leading and trailing edges for upstream and downstream waves. $x_0 = x_L E$ for upstream and $x_0 = x_T E$ for downstream. Legend: ● right moving wave, 1000 Hz; 66

Chapter 1

Introduction

1.1 Literature Review

For people living near the vicinity of an airport, the noise from jet engines can be a big problem. The encroachment of residential zones closer to airport boundaries and the increase of air traffic have made this issue one of the major hurdles for the aircraft industry. To reduce aircraft noise pollution, the commercial jet engine manufacturers, National Aeronautics and Space Administration (NASA), and similar European agencies have identified engine noise reduction as one of their near- and long-term goals. Hence, there is a lot of emphasis on understanding various sources of noise in an aircraft so that the noise emanating from them could be modeled and controlled.

There are various types of noise sources present in an aircraft. The major contributors are propeller and propfan noise, turbomachinery noise, jet noise and airframe noise. The details about these noise sources and noise mitigation strategies are given by Habbard, [1]. Over the last five decades, the jet exhaust noise of aircraft has been substantially reduced. These reductions have highlighted the importance of the various other sources of noise in modern turbofan engines. Thus studies of aircraft noise due to the (i) airframe and the (ii) internal engine turbomachinery and combustor have recently received renewed attention. This thesis focuses on a portion of the internal turbomachinery noise due to the interaction of combustor-produced entropy disturbances with the downstream turbine.

There are two major sources of noise inside gas turbine engines associated with combustor [2,3]. One is the generation of pressure fluctuations due to the unsteady heat release in the region of turbulent combustion in the combustor. This noise, often called direct combustion noise, has

been investigated by many researchers over the years. Early work on the noise from nonpremixed turbulent flames was reviewed by Kumar [4] with more recent experiments by Singh et al. [5] and by Ramamurthy and Patnaik [6] and the large-eddy simulation study by Ihme et al. [7]. Premixed turbulent diffusion flames have been recently examined experimentally by Rajaram and Lieuwen [8, 9] who also provided a reasonable summary of previous experiments on premixed flames. Theoretical studies of direct combustion noise appear to have originated with Bragg [10] who used a heuristic interpretation of the acoustic analogy [11]. Bragg's results were placed on a more solid foundation by Strahle [12] who also used Lighthill's theory. An alternative form of Lighthill's analogy for use in combustion noise was used by Dowling [13].

The second source of noise, and also focus of the present thesis, is the interaction of the unsteady entropy field produced by the combustor with the downstream turbine. This noise is termed indirect combustion noise and has achieved significant analytical investigation [14–18], but limited experimental study [19, 20]. These studies examine the production of noise by the scattering of entropy waves by a flow inhomogeneity, either a convective acceleration due to nozzle contraction or a local region with different acoustic impedances, and have led to considerable insight regarding the fundamental nature of the scattering process. The Lighthill theory [11] of aerodynamic noise is based on an acoustic analogy in which turbulence provides a quadrupole source distribution in an ideal fluid at rest. In the development of the theory Lighthill, and later Ffowcs Williams and Hawkings [21], emphasized the need to take into account the convection of noise source while modeling the radiated sound. The convection of noise source is particularly important in the case of an entropy spot, which is acoustically silent when convecting uniformly, but emits sound when it encounters a flow inhomogeneity. For example, this flow inhomogeneity could be caused by acceleration by a convergent nozzle or presence of a obstacle in the fluid, such as turbine blades. In 1975, Howe [14] developed an analytical model in terms of a renormalized Green's function to examine the generation of sound by aerodynamic sources which are being convected past fixed scattering bodies through a steady mean flow. It is found that the effect of obstacle in equivalent to local distortion of the geometry of the three-dimensional space occupied by the medium, the extent of which governs the acoustic radiation. This model was developed primarily for the analysis of the

sound generated during the inhomogeneous convection of a source of constant strength through a neck in a duct. Later, Ffowcs Williams and Howe [15] applied this analytical theory to examine the sound generated when an inhomogeneity in density is convected in a low Mach number steady flow through a contraction in a duct of infinite extent, and also when the inhomogeneity exhausts through a nozzle into free space. Two extreme cases regarding the structure of the inhomogeneity were studied: first, that in which the inhomogeneity consists of of a slug of fluid of different density from the ambient mean flow, and second, in which the inhomogeneity consists of a small spherical disturbance. It is found that the velocity and Mach number dependence of the sound generated in either case is similar to that of a dipole source. However, this study is limited to low Mach number flows and is applicable for incompressible mean flow only.

In 1977, Marble and Candel [16] presented an analytical model to examine the acoustic signature generated by convection of non-uniform temperature regions or "entropy spots" through a nozzle. The analytical model assumes that all disturbance have wavelengths that are much longer than the nozzle, i.e., the nozzle is compact. Thus, for the disturbances of very long wavelengths, the nozzle appears as a discontinuity in the state of the medium supporting the convection and propagation. The nozzle then provides matching conditions, between uniform upstream and downstream states, which are derived from one-dimensional conservation laws and the geometric description of the nozzle. This model is applicable for subsonic as well as supersonic Mach numbers, however it limits itself to one dimensional flows.

Cumpsty and Marble [22] used the concept of the compact nozzle, introduced by Marble and Candel [16], to develop a two-dimensional theory relating to the interaction of entropy fluctuations, as well as vorticity and pressure, with turbine blade rows. This theory has been termed as "actuator disk theory." It is found that for the interaction of entropy with a blade row to be important, it is essential that the mean pressure change across the blade row should be large, although all unsteady perturbations are assumed small. The actuator disk theory also assumes that the blade pitch-chord ratio is small and radial variations along the blade are negligible such that the flow can be treated as two-dimensional in the developed axial-tangential plane. Most of the literature concerned with combustion noise had either been empirical or was modeled in an essentially one-dimensional

fashion. An essential feature of the this model is that it is two-dimensional. The change from one to two dimensions means that the pressure perturbations are no longer the simple waves traveling directly upstream or downstream at the local speed of sound relative to the flow. Instead a system of spiraling waves is set up, and these waves may either propagate without attenuation or else decay exponentially with axial distance. The decaying waves are referred to as evanescent or, colloquially, cut-off. The angle at which the waves propagate is a function of frequency and wavelength in any prescribed direction. In modeling annular situations the wavelength in the circumferential direction is adopted as an independent variable; then axial wavelength and phase velocity vary with frequency so that the system is frequency dispersive.

In order to understand the relative importance of direct and indirect mechanism of combustion noise, in 1979 Cumpsty [17] used the basic features of the two-dimensional low-frequency actuator disk theory to model the combustion noise generated by unsteady combustion or heat addition by idealizing combustion or heat addition processes to occur over a short distance in the flow direction. The model predicted the amplitude and phase of pressure, entropy and vorticity perturbations produced by small amplitude fluctuations in the heat addition. It is observed that pressure waves propagate away from the heat input region upstream and downstream, whilst vorticity and entropy waves are convected downstream with the mean flow. Strong resonant peaks in the pressure and vorticity waves are observed close to cut-off condition of the pressure waves in two dimensions, similar to what Cumpsty and Marble [22] had reported. Cumpsty provides estimates of the magnitude of both the entropy and pressure perturbations from a model of the combustion process and confirms that the generation mechanisms of the two types of disturbances are essentially inseparable. He also argues that indirect combustion noise mechanism predominates the direct mechanism for modern turbine engines with many stages.

In 2009, Leyko et al. [23] extended Marble and Candel's [16] work to allow for normal shocks in the nozzle. They used the one dimensional analytical method combined with numerical tools to show that the ratio of indirect to direct combustion noise is high in actual aero-engines, but low in most laboratory combustion chambers. This is due to the fact that combustion chambers in laboratories are not followed by a strong mean flow acceleration, and therefore indirect noise is

negligible in those configurations.

According to Bake, Michel and Rohle [24], a proper analytical understanding of the indirect combustion noise is still lacking and can be obtained by a comparison of theoretical predictions with careful experiments. Out of all the experiments performed till now concerning combustion noise, the one performed by Bake et al. [19] is at the moment the only one focused specifically on indirect combustion noise. They performed a series of canonical experiments using an "entropy wave generator". These involved the measurement of the sound generated during controlled high speed convection of a slug of hot gas through a converging−diverging nozzle. The hot slug is regarded as an idealized product of combustion, and it is argued that a study of the sound-source mechanism in this case should provide an improved insight into the sound generation process of a real inhomogeneous combustion outflow. Bake et al. [20] asserted that indirect combustion noise is dipole in character and that its mechanism of generation must be similar to that produced by turbulence and other vortex sources in confined flows, so that the overall contributions from the two sources are not independent and should not be considered in isolation. However, their numerical simulations were incapable of quantifying the separate effects of the entropy and vortex sources in their experiment. But according to Bake et al. [19], predictions based on Marble and Candel's one dimensional theory are too low at nozzle Mach numbers less than about 0.6 and too high when nozzle Mach number exceeds 0.7. Inspired by these experiments, Howe [25] carried out a theoretical work to determine the indirect combustion noise generated when an ideal slug of hot gas convects at high subsonic speed through a converging-diverging nozzle where he argues about the specific Mach number dependence observed in Entropy Wave Generator (EWG) experiments.

These experiments, called the Entropy Wave Generator (EWG), were also used by Leyko et al., [26] to validate the analytical tools created by Marble and Candle [16] in the supersonic case, showing that indirect combustion noise can be correctly predicted using the analytical method. For supersonic case they found that indirect noise dominates over direct noise. Duran and Moreau [27] carried forward the numerical and analytical tests for EWG experiment for subsonic cases. They found that direct combustion noise has an important effect in the global noise generated and can not be neglected with respect to the indirect noise. In auxiliary power units, which are significantly

different from turbofan engines, it has been established that direct combustion noise dominates, [28], but a similar statement concerning turbofans has not been established yet and research is ongoing [29]. Kings et al. [30] recently carried out experimental investigations for indirect combustion noise due to artificial vorticity fluctuations. Cumpsty [17], based on his low-frequency actuator disk approach, argued that indirect noise could dominate. However, these arguments have not been independently verified. It is also worthwhile to note that actuator disk theories provide only transfer function estimates from the combustor-induced disturbances to the nozzle exit pressure fluctuations and thus must rely on (semi)empirical data for estimating absolute levels.

The relative importance of the direct and indirect noise mechanisms in the combustion noise is not yet known completely. As a step toward further improving the understanding of the indirect noise mechanism and, hence, toward addressing the larger question of its importance relative to the direct mechanism, Bodony previously investigated the noise generated by an isolated body interacting with an entropy disturbance [31]. Direct numerical simulations were carried out for an imposed entropy disturbance impinging on a symmetric NACA 0012 airfoil for variety of disturbance profiles. The direct sound radiation was captured and compared with the indirect sound predicted using a linear theory. The current work is the extension of this previous work to a linear cascade of cambered turbine blades. In this report, computational results for interaction of an entropy disturbance with stator vanes and analysis of the resulting sound field are presented. Further, comparative studies are carried out between the DNS results and those predicted by the actuator disk theory. The entropy disturbance has been simulated using both low-frequency plane-waves and high frequency localized pulses, as done previously by [15].

1.2 The structure of the thesis

The actuator disk theory, along with its analytical details, is discussed in the chapter 2 while reproducing the key results through numerical implementation of the theory. The subsequent chapter presents the details of direct numerical simulations for plane-wave entropic disturbances and compares them against those predicted by the actuator disk theory. Discussion on various

aspects of comparison follows. In chapter 4, DNS results are presented corresponding to an entropy fluctuation in terms of a localized high frequency hot-spot. A comparative study of the DNS results and those predicted by actuator disk theory follows. Finally, in Chapter 5, the thesis concludes with a summary and suggestions for future work.

Chapter 2

Actuator disk theory

By the mid 1970s, it was generally accepted that jet propulsion engines produce more noise from their exhaust than could be accounted for by jet noise alone. The extra noise is known variously as excess, tailpipe, or core noise and becomes more important only at low jet velocities; the lower aircraft speed reduces the jet noise and therefore increases the relative importance of other sources. Researchers have found that much of the extra noise coming from the exhaust of the engine is associated with the combustor.

There are two major sources of noise inside gas turbine engines associated with the combustor. One is the generation of pressure fluctuations due to the unsteady heat release in the region of turbulent combustion in the combustor. This noise, often called direct combustion noise, has been investigated by many researchers over the years [4, 5, 7, 10, 12]. The second source of noise is the interaction of the unsteady entropy field produced by the combustor with the downstream turbine. This noise is termed as indirect combustion noise and has achieved significant analytical investigation. In 1977, Cumpsty and Marble [22] developed an analytical theory, named actuator disk theory, to predict indirect combustion noise. The key assumptions and features of the model given in the original text [22], are reproduced here:

(a) The blade passages are assumed sufficiently short compared with the wavelength that there is no phase difference between the flow quantities on the upstream and downstream sides of the blade row. The flow inside the blade row may therefore be treated as steady, and solutions upstream and downstream may be obtained by matching mass flow, total pressure and entropy across the row.

(b) The blade pitch-chord ratio is assumed to be low, which is equivalent to assuming that the blades are replaced by a very large number of equivalent short ones. This means that the blading details can be ignored and only inlet and outlet flow Mach number and direction need be considered. Any information, at or around the blade passing frequency must therefore be excluded. In real engines, blade passing frequency is much higher than the frequency associated with entropy fluctuations. The restriction to low frequencies here and in (a) above allows rotor blade to be treated in exactly the same way as stators after allowing for the change in mean flow Mach number and direction relative to the rotor.

(c) Although the entropy and pressure perturbations are small compared with the corresponding time mean quantities, the deflection and acceleration of the mean flow are generally large. This is essential for modeling the phenomenon, since only when the mean flow-changes through a blade row are large does an entropy perturbation produce a significant pressure perturbation.

(d) The axial flow is taken to be subsonic. Although this condition can be relaxed, there seems to be no practical interest in turbines with supersonic axial flows.

(e) The radial variations along the blades are neglected and the flow is treated as two-dimensional in developed axial-tangential plane.

(f) Although the blades are assumed to be vanishingly short, the overall axial length of the turbine is obtained by allowing appropriate axial gaps between blade rows, and is not necessarily short compared with the relevant wavelengths.

(g) When the entropy wave interacts with the blade row, pressure waves are propagated away from the row upstream and downstream, while vorticity is convected downstream.

Now that key assumptions and features of the actuator disk theory are stated, analytical details of the theory should follow. Analytical details, implementation of the theory, and some of the key results have been discussed in the section below.

2.1 Characteristic of the actuator disk

As wavelengths of the disturbances considered here are much larger than blade chord, the characteristics of the cascade constitute matching conditions between the flow fields upstream and downstream of the blade row. Three of the four matching conditions are:

(i) conservation of entropy, indicating that the perturbations do not change the losses across the blade.

(ii) continuity of mass flow, as blade rows have no capacitance.

(iii) conservation of stagnation enthalpy in a coordinate system fixed with the blade rows.

The fourth condition depends on the blade outlet Mach number. For subsonic flow a condition on the gas efflux angle with respect to the blade row is imposed, while in supersonic outlet flow, a choking condition is used instead.

These matching conditions are applied in terms of the non-dimensional variables $\frac{s'}{c_p}$, $\frac{p'}{\gamma p}$, $\frac{w'}{a}$, and θ'. Assuming that blade row exists at $x = 0$ and denoting the states upstream and downstream of the blade row by subscripts 1 and 2, the entropy conservation law, is:

$$\frac{s'_1}{c_p} = \frac{s'_2}{c_p} \tag{2.1}$$

Thermal properties of the fluid have been assumed to be constant throughout the domain. In case of substantial losses, such as occurrence of stall or presence of shocks, the above relation becomes complex. These complexities have been ignored here as passages have been assumed to be free of significant losses.

The continuity of mass flow leads to the following conservation equation;

$$\frac{\rho'_1}{\rho_1} + \frac{w'_1}{W_1} - \theta'_1 \tan\theta_1 = \frac{\rho'_2}{\rho_2} + \frac{w'_2}{W_2} - \theta'_2 \tan\theta_2 \tag{2.2}$$

The density perturbations in equation (2.2) can be eliminated in favor of the pressure and entropy changes by using the equation (2.3)

$$\frac{s'}{c_p} = \frac{p'}{\gamma p} - \frac{\rho'}{\rho} \tag{2.3}$$

On using equation (2.1) and equation (2.3), mass conservation equation leads to the following relation

$$\frac{p_1'}{\gamma p_1} + \frac{1}{M_1}\frac{w_1'}{a_1} - \theta_1' \tan\theta_1 = \frac{p_2'}{\gamma p_2} + \frac{1}{M_2}\frac{w_2'}{a_2} - \theta_2' \tan\theta_2 \tag{2.4}$$

The conservation of the stagnation enthalpy coupled with linearized equation of state is given by the following equation,

$$\frac{1}{1+\frac{1}{2}(\gamma-1)M_1^2}\frac{p_1'}{\gamma p_1} + M_1\frac{w_1'}{a_1} + \frac{s_1'}{(\gamma-1)c_p} = \frac{1}{1+\frac{1}{2}(\gamma-1)M_2^2}\frac{p_2'}{\gamma p_2} + M_2\frac{w_2'}{a_2} + \frac{s_2'}{(\gamma-1)c_p} \tag{2.5}$$

The final matching condition is chosen depending upon whether the outlet Mach number relative to the turbine blade row is subsonic or supersonic. If outlet velocity is subsonic, the discharge flow angle is an appropriate quantity to describe. Owing to the Kutta condition, the fluctuations in discharge angle should vanish, thus;

$$\theta_2' = 0 \tag{2.6}$$

When the discharge is supersonic with respect to the turbine blade row choking condition gives the final matching condition, as nozzles of interest in this study are not choked and have subsonic discharge velocities these results are being omitted here and can be found in reference [22].

2.2 Analytical details

Each of the two-dimensional flow fields, upstream and downstream, of a single compact turbine cascade, is described in the undisturbed state by a constant gas speed, W, in a direction, θ, uniform pressure, p, and density, ρ. The disturbances to this uniform field may originate upstream, downstream, or at the cascade itself. These disturbances consist of two waves being convected with the mean flow; the vorticity, $\xi' = \frac{\partial v'}{\partial x} - \frac{\partial u'}{\partial y}$ and the entropy, s', and the acoustic waves. These waves are independent of each other to the first order, and hence can be superimposed. The governing equations for the wave system are linearized continuity and momentum equations. Solving these equations results in the following governing relations for the wave structure of the system. A plane entropy wave whose normal makes an angle ν_s with respect to the x- axis, with scalar wavenumber k_s and angular frequency ω, is given by the following equation

$$\frac{s'}{c_p} = \sigma \exp\left\{i\left[\omega t - k_s(x\cos\nu_s + y\sin\nu_s)\right]\right\} \tag{2.7}$$

The above entropy wave will satisfy the governing linearized continuity and momentum equations if following dispersion relation is satisfied,

$$\frac{ak_s}{\omega} M\cos\left(\nu_s - \theta\right) = 1 \tag{2.8}$$

where, $M = W/a$ is the local Mach number. The entropy wave is accompanied by no velocity field, $u'_s = v'_s = 0$, and no pressure field, $p'_s = 0$. In the absence of a pressure field, the density field is associated with the entropy disturbance by,

$$\frac{\rho'_s}{\rho} = -\frac{s'}{c_p}. \tag{2.9}$$

The perturbation vorticity wave with normal direction ν_ξ and scalar wavenumber k_ξ can be written as,

$$\xi' = \xi \exp\left\{i\left[\omega t - k_\xi(x\cos\nu_\xi + y\sin\nu_\xi)\right]\right\} \tag{2.10}$$

The direction, ν_ξ, and scalar wavenumber, k_ξ, are related to the angular frequency through the following dispersion relation,

$$\frac{ak_\xi}{\omega} M \cos\left(\nu_\xi - \theta\right) = 1. \tag{2.11}$$

The vorticity carries no pressure disturbance [22] and, because there is an independent entropy perturbation, no generality is lost in taking $\rho'_\xi = 0$. Under these assumptions, the resulting perturbation in velocity magnitude, w'_ξ and disturbance to flow angle, θ'_ξ, due to perturbation vorticity is obtained by solving the linearized continuity and momentum equations [22]. The non-dimensional perturbation in velocity magnitude is given as,

$$\frac{w'_\xi}{a} = -\,i\,\frac{\xi}{ak_\xi} M \sin\left(\nu_\xi - \theta\right) \exp\left\{i\left[\omega t - k_\xi(x\cos\nu_\xi + y\sin\nu_\xi)\right]\right\} \tag{2.12}$$

and the disturbance to flow angle, θ'_ξ, is obtained as,

$$\theta'_\xi = i\,\frac{\xi}{ak_\xi} M \cos\left(\nu_\xi - \theta\right) \exp\left\{i\left[\omega t - k_\xi(x\cos\nu_\xi + y\sin\nu_\xi)\right]\right\}. \tag{2.13}$$

The entropy and vorticity waves are described by independent solutions, hence no generality is lost in considering acoustic waves to be irrotational and isentropic. An acoustic wave with scalar wavenumber k and wave normal inclined at ν to the axial direction given as,

$$\frac{p'}{\gamma p} = p^\nu \exp\left\{i\left[\omega t - (k_x x + k_y y)\right]\right\} \tag{2.14}$$

satisfies the governing equation if the following dispersion relation is satisfied

$$\left(1 - \frac{ak_x}{\omega} M\cos(\theta) - \frac{ak_y}{\omega} M\sin(\theta)\right)^2 - \left(\frac{ak_x}{\omega}\right)^2 - \left(\frac{ak_y}{\omega}\right)^2 = 0. \tag{2.15}$$

The above dispersion relation, equation (2.15), admits complex values of k_x and k_y. As equation (2.14) demonstrates, complex wavenumbers are associated with attenuated solutions rather than waves. The turbine periphery of a linear cascade will lead to periodic solutions in y-direction

and, hence, permissible values for k_y are real. The axial wavenumber k_x can be complex and in general it is appropriate to write,

$$k_x = k_x^1 \pm i k_x^2.$$

The corresponding pressure disturbance is,

$$\frac{p'}{\gamma p} = p^{\nu,\pm} \exp\{i\,[\omega t - (k_x^1 \pm i k_x^2)x - k_y y]\}. \tag{2.16}$$

It is convenient to define a vector $k_x^1 = k^1 \cos\nu$, $k_y = k^1 \sin\nu$, normal to the plane disturbance so that the corresponding velocity and angle perturbations are,respectively

$$\frac{w'_a}{a} = \frac{(ak^1/\omega)\cos(\nu-\theta) + \cos\theta(\pm i a k_x^2/\omega)}{1 - M\{(ak^1/\omega)\cos(\nu-\theta) + \cos\theta(\pm i(ak_x^2/\omega))\}} p^{\nu,\pm} \exp\{i\alpha^{\pm}\} \tag{2.17}$$

and

$$\theta'_a = \frac{1}{M} \frac{(ak^1/\omega)\sin(\nu-\theta) - \sin\theta(\pm i a k_x^2/\omega)}{1 - M\{(ak^1/\omega)\cos(\nu-\theta) + \cos\theta(\pm i(ak_x^2/\omega))\}} p^{\nu,\pm} \exp\{i\alpha^{\pm}\} \tag{2.18}$$

where $\alpha^{\pm} = \omega t - (k_x^1 \pm i k_x^2)x - k_y y$. The above expressions for velocity and flow angle disturbance correspond to complex valued wavenumbers and thus can consist of both attenuated and wave-like solutions.

After having established the disturbance field caused by entropy, vorticity and acoustic waves, the interaction of the wave system with turbine blade rows should be studied using governing matching conditions. Selection of the appropriate set of solutions may be divided into two steps: the classification of acoustic waves according to their direction of travel; and solving the governing equations 2.1, 2.2, 2.5 and 2.6 by linearly superimposing the disturbance fields created by the entropy, vorticity and acoustic waves.

The flow across a turbine cascade may be disturbed by an entropy or vorticity wave convected from upstream or by an acoustic wave originating either upstream or downstream of the blade row. The resulting interaction with turbine blade row will generally involve all three types of

waves, regardless of the initiating disturbance, each having a common peripheral wavenumber $k_y = k\sin\nu = k_s \sin\nu_s = k_\xi \sin\nu_\xi$. Thus, from the dispersion relations given by equations (2.8) and (2.11),

$$\frac{ak_s}{\omega}\cos\nu_s = \frac{ak_\xi}{\omega}\cos\nu_\xi = \frac{1-(ak_y/\omega)M\sin\theta}{M\cos\theta} \tag{2.19}$$

For the acoustic waves, the dispersion relation, equation (2.15), is quadratic, so that the values of ak_x/ω are;

$$\frac{ak_x}{\omega} = \frac{-M\cos(\theta)(1-(ak_y/\omega)M\sin\theta)}{1-M^2\cos^2\theta} \pm \left\{\frac{(1-(ak_y/\omega)M\sin\theta)^2 - (1-M^2\cos^2\theta)(ak_y/\omega)^2}{(1-M^2\cos^2\theta)^2}\right\}^{\frac{1}{2}} \tag{2.20}$$

In order to construct solutions one must know whether value of k_x obtained is real or complex and whether acoustic wave moves upstream or downstream. When k_x is real, an acoustic wave is generated by a disturbance moving along the turbine cascade whose wave front has supersonic relative velocity. If the value of k_x is complex, it leads to attenuated solutions. The limiting value of such k_x is referred as cut-off. Since the pressure wave propagate at a speed a relative to the gas moving at velocity W the direction of propagation along the turbine axis may be found by considering the sign of net axial velocity component, $W\cos\theta + a\cos\nu$. The pressure waves moves downstream when this is positive and upstream when negative.

Now, we have all the relevant information available to us in order to solve the governing equations given by equations (2.1, 2.4, 2.5 and 2.6). For an incoming entropic wave disturbance upstream of the stator vane, these governing governing equations form a system of linear equations,

$$\mathbf{B}_I\mathbf{V}_I = \mathbf{B}_o\mathbf{V}_o \tag{2.21}$$

where,

$$\mathbf{V}_I = \left[\frac{s_1'}{c_p} \quad \frac{p_1'^+}{\gamma p_1} \quad \frac{p_2'^-}{\gamma p_2} \quad \frac{\xi_1'}{a_1 k_\xi}\right]^T, \tag{2.22}$$

$$\mathbf{B}_I = \begin{bmatrix} 1 & 0 & 0 & 0 \\ -1 & 1+\frac{1}{M_1}\frac{w'^{+}_{a_1}}{a_1} - \theta'^{+}_{a_1}\tan\theta_1 & -1-\frac{1}{M_2}\frac{w'^{-}_{a_2}}{a_2} + \theta'^{-}_{a_2}\tan\theta_2 & \frac{1}{M_1}\frac{w'_{\xi_1}}{a_1} \\ \frac{\beta_1}{\gamma-1} & \beta_1 + \beta_1 M_1 \frac{w'^{+}_{a_1}}{a_1} & -\beta_2 - \beta_2 M_2 \frac{w'^{-}_{a_2}}{a_2} & \beta_1 M_1 \frac{w'_{\xi_1}}{a_1} \\ 0 & 0 & -\theta'^{-}_{a_2} & 0 \end{bmatrix}, \tag{2.23}$$

$$\mathbf{V}_o = \begin{bmatrix} \frac{s'_2}{c_p} & \frac{p'^{+}_2}{\gamma p_2} & \frac{p'^{-}_1}{\gamma p_1} & \frac{\xi'_2}{a_2 k_\xi} \end{bmatrix}^T, \tag{2.24}$$

and

$$\mathbf{B}_o = \begin{bmatrix} 1 & 0 & 0 & 0 \\ -1 & 1+\frac{1}{M_2}\frac{w'^{+}_{a_2}}{a_2} - \theta'^{+}_{a_2}\tan\theta_2 & -1-\frac{1}{M_1}\frac{w'^{-}_{a_1}}{a_1} + \theta'^{-}_{a_1}\tan\theta_1 & \frac{1}{M_2}\frac{w'_{\xi_2}}{a_2} \\ \frac{\beta_2}{\gamma-1} & \beta_2 + \beta_2 M_2 \frac{w'^{+}_{a_2}}{a_2} & -\beta_1 - \beta_1 M_1 \frac{w'^{-}_{a_1}}{a_1} & \beta_2 M_2 \frac{w'_{\xi_2}}{a_2} \\ 0 & 0 & -\theta'^{-}_{a_1} & 0 \end{bmatrix}. \tag{2.25}$$

Superscripts $^+$ and $^-$ correspond to downstream and upstream traveling pressure waves, respectively. Subscripts $_1$ and $_2$ correspond to upstream and downstream locations with respect to the compact stator vane. Subscripts $_a$ and $_\xi$ correspond to acoustic disturbance and vorticity disturbance, respectively and Greek variable β_i is defined as:

$$\beta_i = \frac{1}{1 + \frac{1}{2}(\gamma - 1)M_i^2} \tag{2.26}$$

Solving the above system of equations for a given set of mean flow conditions, we can reproduce the actuator disk results. Sample results given by Cumpsty and Marble for an isolated blade row of stator vanes have been reproduced in the following section.

2.3 Reproduction of results of ADT

2.3.1 Isolated blade row: stator vane

Our initial objective is to reproduce the results obtained by Cumpsty and Marble [22]. For the left and right hand wave systems, the amplitude and phase of upstream and downstream going pressure waves and the vorticity wave are calculated for an input consisting of entropy waves. The results shown here will consist of pressure waves due to entropy wave inputs on an isolated blade row. In representing the results it is convenient to take $\frac{fY}{a}$ as the independent variable, where f is the frequency, Y is the azimuthal wavelength along the cascade and a is the speed of the sound in the flow into the blade row. The blade row typifies a nozzle guide vane with a low Mach number, $M_1 = 0.20$, axial inlet flow and a high subsonic outlet flow, $M_2 = 0.95$, inclined at a large angle to the axial direction, $\theta_2 = 70.4^o$. A MATLAB code was written to implement the actuator disk theory for a single blade row. It is observed that the peak occurs at the point of cut-off. The waves below cut-off are attenuated. Results obtained by numerical implementation of ADT are compared against those given by Cumpsty and Marble both downstream and upstream of the blade. Comparison between the two ADT implementations is shown in the figures(2.1, 2.2) for downstream and upstream axial locations, respectively. These figures show the ratios of the pressure perturbation amplitude to the entropy amplitude for the upstream and downstream sides of the blade row. It is observed that numerical implementation is consistent and is able to reproduce the analytical results given by Cumpsty and Marble both upstream and downstream of the blade.

Having successfully reproduced the results given by Cumpsty and Marble, our next objective

is to validate these results against those obtained by direct numerical simulation of an entropic disturbance added upstream of a stator vane. The computational results have been obtained for entropic disturbance in the form of low-frequency plane waves as well as high frequency localized pulses. The details of these computations are given in the following chapters.

2.4 Figures for chapter 2

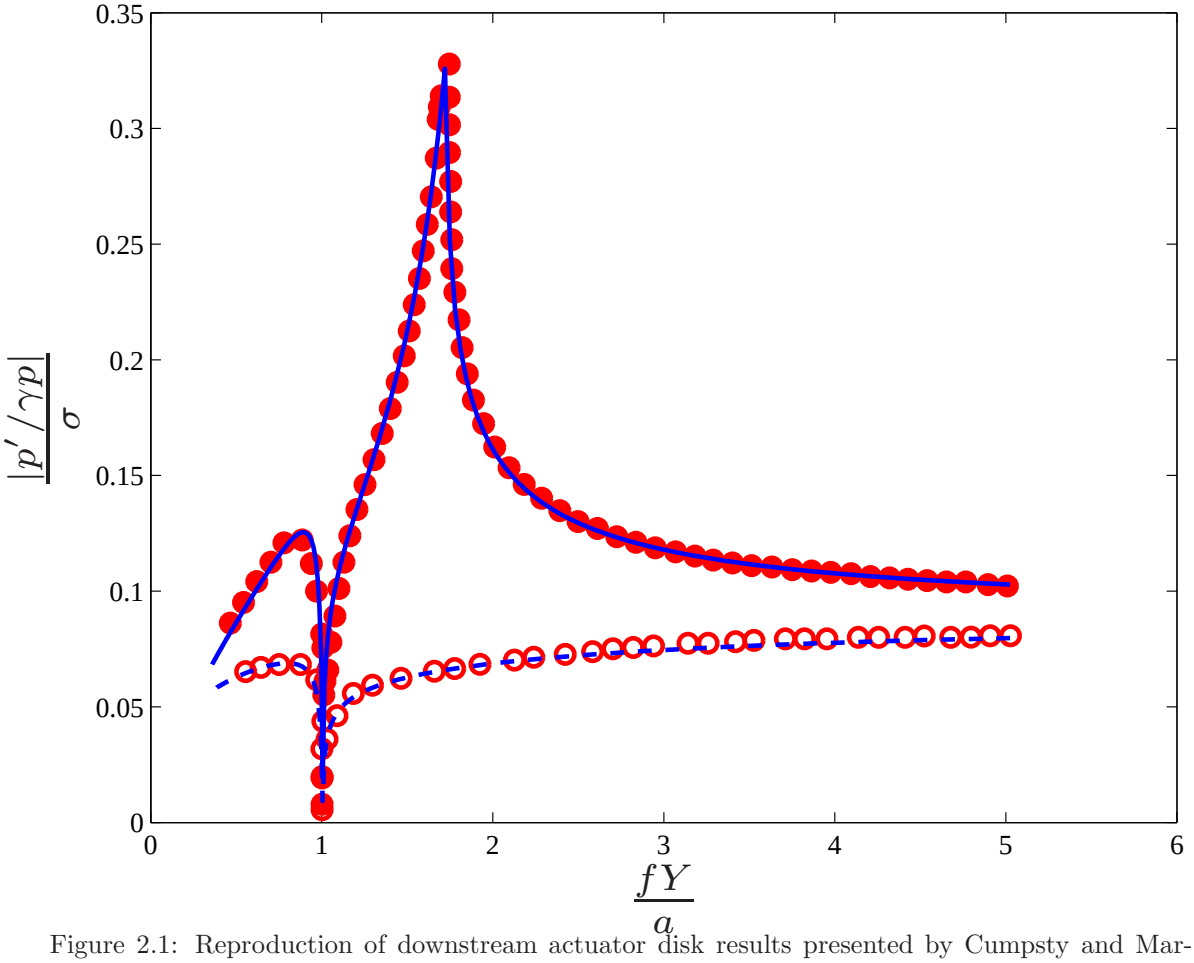

Figure 2.1: Reproduction of downstream actuator disk results presented by Cumpsty and Marble [22]. $M_1 = 0.20$, $\theta_1 = 0^o$, $M_2 = 0.95$, $\theta_2 = 70.4^o$. Legend: ● original result for right moving pressure wave; ○ original result for left moving pressure wave; — reproduced result for right moving pressure wave; – – – reproduced result for left moving pressure wave.

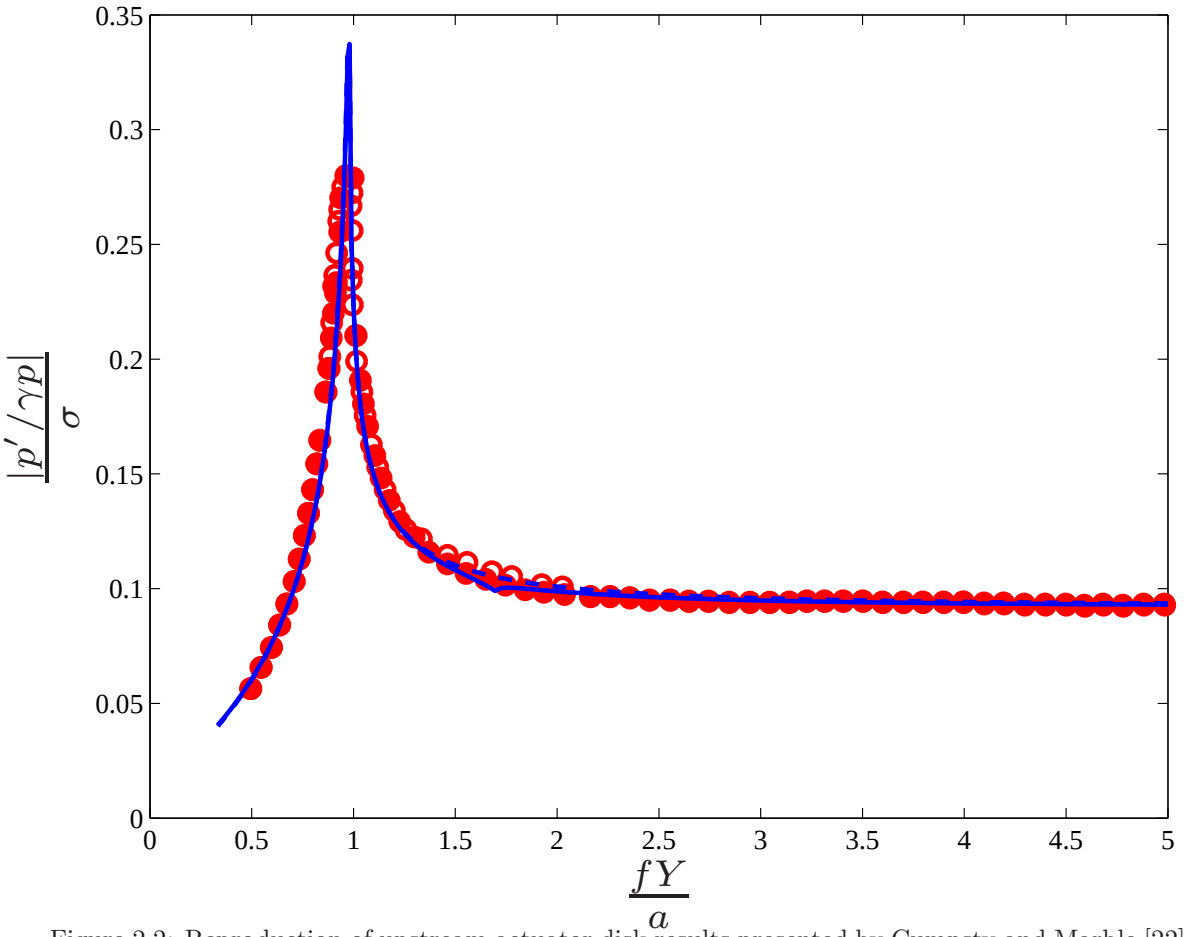

Figure 2.2: Reproduction of upstream actuator disk results presented by Cumpsty and Marble [22]. $M_1 = 0.20$, $\theta_1 = 0^o$, $M_2 = 0.95$, $\theta_2 = 70.4^o$. Legend: • original result for right moving pressure wave; ▫ original result for left moving pressure wave; — reproduced result for right moving pressure wave; – – – reproduced result for left moving pressure wave.

Chapter 3

Direct numerical simulation of entropy disturbance scattering into sound

3.1 Computational details

The NASA "Combustor Exit Radial Temperature Simulator" (CERTS) geometry [32,33] was chosen as the test candidate for the current simulations because the flow conditions are representative of an actual engine environment and the geometry is publicly available. The CERTS test turbine was a 0.767 scale rig modeling of the first stage of a two-stage core turbine designed for modern high bypass ratio engines. The vane has an untwisted constant-chord section, and was designed for a constant exit flow angle of 75 deg from the axial direction. The rotor leading edge was designed to accept the vane exit flow with either zero or small negative incidence. Using the geometric details provided by Stabe et. al. [32], the computational domain, along with the CERTS stator, is sketched in figure 3.1.

An overset (chimera) grid approach is used to simulate the geometry. The fluid is assumed to be inviscid with slip walls on the surface of airfoil and periodic boundary conditions on top and bottom boundaries of the computational domain, similar to the approach used previously [31]. The periodic spacing corresponds to the CERTS inter-blade spacing at the 75% radius giving an effective two-dimensional cascade representation of the stator blade row. The left and right boundaries of the background domain are the inlet and outlet, respectively. The compressible Euler equations are solved on the curvilinear mesh surrounding the airfoil using an approach used earlier by Bodony [31]; the 'background' grid which surrounds the blade uses a globally fifth order finite difference scheme which is fourth order accurate along the boundaries and eighth order accurate in the interior, while a second-order explicit finite difference scheme is used along the small blade-conforming mesh.

Flow conditions given in the table 3.1 and table 3.2 have been simulated for the CERTS stator vane.

Table 3.1: Freestream flow conditions: CERTS turbine

Inlet total temperature	672.2 K
Inlet total pressure	310300 Pa

Table 3.2: Freestream flow conditions: modern turbine

Inlet total temperature	1073.7 K
Inlet total pressure	483815.5 Pa

3.2 Numerical method

The simulation to which the ADT predictions are to be compared solved the Euler equations in generalized coordinates $\xi = \Xi(x)$ according to

$$\frac{\partial}{\partial t}\left(\frac{\rho}{J}\right) + \frac{\partial}{\partial \xi_j}(\rho U_j) = 0 \tag{3.1}$$

$$\frac{\partial}{\partial t}\left(\frac{\rho u_i}{J}\right) + \frac{\partial}{\partial \xi_j}(\rho u_i U_j + p\hat{\xi}_{j,i}) = 0 \tag{3.2}$$

$$\frac{\partial}{\partial t}\left(\frac{\rho E}{J}\right) + \frac{\partial}{\partial \xi_j}(\{\rho E + p\}U_j) = 0 \tag{3.3}$$

where $J = |\frac{\partial x}{\partial \xi}|$ is the Jacobian of the grid transformation, $\hat{\xi}_{j,i} = J^{-}1\frac{\partial \xi_j}{\partial x_i}$ are the Jacobian-wighted matrices, and $Ui = uj\hat{\xi}_{j,i}$ are the contravariant velocities. When the equations are non-dimensionalized with respect to the ambient density ρ_∞, the ambient speed of sound a_∞, the stator blade chord, c the equation o state for a calorically perfect ideal gas is

$$p = \frac{\gamma - 1}{\gamma} \rho T \tag{3.4}$$

with $\gamma = C_p/C_v$, the ratio of specific heats, fixed at 1.4.

The equations are discretized using a node-centered finite difference approach of the form

$$\frac{\partial}{\partial \xi} \approx P^{-}1Q \tag{3.5}$$

where P, Q are explicit summation-by-parts matrices that are eighth order accurate in the interior and fifth order accurate globally [34]. Simultaneous approximation-term boundary conditions are used on all computational non-periodic boundaries to enforce slip [35] and far-field [36] conditions. These boundary conditions are numerically stable and have been shown to be accurate in aeroacoustic problems [37]. A sponge region located adjacent to the inlet and outlet boundaries is also used to help impose the incident sound waves and to further reduce unwanted reflections [38].

Two overset grids, were used for the main turbine passage and the region immediately adjacent to the blade. The overset grids utilize high-order Lagrange polynomial interpolation for passing flow data between them [39]. Determination of the overlap points and interpolation stencils uses the pre-processing tool Bellero developed at Wright-Patterson AFB [40]. While accurate, the use of Lagrange polynomial interpolations can generate numerical instabilities which are not dissipated by the centered finite difference scheme. We thus use a high-order, optimized implicit filter [41] with free parameter $\alpha_f = 0.49$. Near computational boundaries the filter stencil becomes biased.

3.3 Grid converged mean flow

The flow conditions given in table 3.1 and table 3.2 are representative of the CERTS operating condition and that of modern turbine engines, respectively. With these flow conditions, the compressible Euler equations are solved until the flow established itself around the airfoil and until the ambient pressure-field was sufficiently steady. Figure 3.2 shows the grid-converged flow over CERTS stator vane having 1.2 million grid points with freestream flow conditions of table 3.1.

Pressure fluctuations in the mean flow were measured at upstream and downstream stations to make a conclusion regarding steadiness of the ambient flow field. Figure 3.3(a) and figure 3.3(b) demonstrate the difference in non-dimensional mean flow pressure between the two grids, having 0.3 and 1.2 million grid points, at the upstream and downstream probe stations, respectively. All the computations to follow are corresponding to the finer grid having 1.2 million grid points.

The periodic domain allows sound to travel, without dissipation, transversely to the mean flow and a perfectly quiet flow is not achievable in a reasonable amount of time, thus special post-processing techniques are used to extract the entropy-generated sound. Once the flow around the vane was sufficiently steady, an entropic disturbance was added to the freestream. To analyze the pressure perturbations created by the entropy disturbance alone, the mean flow was subtracted from all the test cases.

3.4 Plane-wave entropic disturbance

Once the flow around the vane was established, an entropic disturbance was added to the freestream in the form of a plane wave. The interaction of an incoming plane-wave of entropy disturbance with turbine blades was simulated using the parameters specified in table 3.3 for CERTS operating condition given in table 3.1.

Table 3.3: Parameters for direct simulation: Entropy disturbance as a plane-wave

Run	σ	Frequency (Hz)	M_∞
pw1	0.10	1000	0.10
pw2	0.10	700	0.10
pw3	0.10	400	0.10
pw4	0.10	1100	0.10

Where, test cases pw1, pw2 and pw3 correspond to a planar entropy wave, $k_y = 0$, whereas test

case pw4 carries a nonplanar input entropy wave. The nonplanar entropy wave has plane-mode and first mode in equal proportions.

To demonstrate a sample interaction, consider a particular disturbance case, pw1, from table 3.3. Let $\rho_0(x)$ be the steady state density field. Then define the difference between the current density and its steady-state value, $\rho' = \rho - \rho_0$. Let $p_0(x)$ be the steady state pressure field. Then define the difference between the current pressure and its steady-state value, $p' = p - p_0$.

A time sequence of four views of the density disturbance $\rho - \rho_0$ (as isolines) and disturbance pressure $p - p_0$ (as contours), corresponding to test case pw1, is shown in figure 3.4. The resulting pressure perturbation at upstream and downstream probe stations, figure 3.5, is captured in 3-dimensional plots which depict the temporal and azimuthal wave nature of pressure perturbations. For illustrative purposes, 3-D plots corresponding to case pw1 are shown in figures 3.6 and 3.7. It is observed that the pressure waves lose their azimuthal variation and become more and more planar as they move farther upstream and downstream of the blade.

Similar results were obtained for other test cases mentioned in table 3.3, visually the results are not very different between all the test cases and hence pressure and density contours and 3-dimensional depiction of pressure waves is omitted for the other test cases. Comparison between the DNS results and those predicted by ADT has been presented in the next subsection.

3.4.1 Comparison of DNS results with ADT

DNS results of the test cases presented in table 3.3 for the operating condition given in table 3.1 are compared against those predicted by the actuator disk theory for an isolated blade row of CERTS stator vane. The upstream and downstream conditions used in ADT calculations are given in table 3.4. Upstream and downstream flow Mach numbers and flow directions have been obtained by taking average of the corresponding values obtained at all the upstream and downstream probe stations, shown in figure 3.5, respectively.

Pressure fluctuations obtained from the ADT are in wavenumber space and hence it is beneficial to convert the pressure signals obtained by DNS to wavenumber space using Fourier transforms. The computational domain is periodic in azimuthal direction, thus no postprocessing of the pressure

Table 3.4: Upstream and downstream flow parameters for ADT

location	M	θ (deg)
Upstream	0.10	0
Downstream	0.48	-74.03

signal is needed to obtain Fourier transforms of azimuthal variation. However, temporal response becomes periodic only after the transient phase has elapsed. In order to eliminate this transient phase appropriate windowing function was selected for the signals. A typical windowing function used is $\frac{1+tanh(5*(t_f-t_0))}{2}$, where t_0 and t_f are initial and final time between which the periodic signal is obtained. The two dimensional Fourier transform of this windowed periodic pressure signal is calculated in order to understand the temporal and azimuthal spectra of the pressure fluctuations and hence noise. This process is repeated for all the test cases of table 3.3, namely for waves of 1000 Hz, 700 Hz, 400 Hz corresponding to planar entropy wave input as well as for nonplanar entropy wave input of 1100 Hz.

Comparisons have been made at various upstream and downstream probe stations for entropy waves of test cases pw1, pw2, pw3 and pw4. The various probe stations are shown in figure 3.5. These probe locations have been used to compare DNS and ADT results shown in figures 3.8 and 3.9. Consider first the downstream results starting with the nearest probe station from the blade. It is observed that the pressure amplitude at the smallest values of fY/a match well with the ADT. As fY/a increases, the DNS results start deviating from ADT results and invariably show higher pressure perturbation amplitudes. This trend continues till the first permissible non-plane mode. As far as plane mode ($k_y = 0$) is concerned, it is observed that DNS values are frequency dependent whereas ADT predicts plane-mode to be independent of the incoming temporal frequency. The upstream and downstream plane mode values are given in the tables 3.5 and 3.6, respectively. The plane mode values obtained by DNS do not show any particular trend with incoming frequency but are quite close to the values predicted by ADT. In general, it is observed that lower frequencies

have higher amplitudes for non-planar azimuthal modes, which is in congruence with the ADT.

If we go further downstream, we observe that all the non-planar azimuthal modes decay exponentially with downstream distance. ADT predicts that all the modes below cut-off will decay exponentially due to subsonic phase velocity which leads to complex valued axial wavenumber, k_x and hence the decay. It is interesting to note that in the present computational set-up all the permissible non-plane modes are below cut off. Further, we see that all the modes below cut-off follow an exponential decay as predicted by the actuator disk.

Now, consider the upstream variation. Starting with closest upstream station of the blade, we observe that unlike downstream behavior, smaller values of fY/a have lower pressure fluctuation than predicted by ADT. Whereas, planar azimuthal mode of DNS results have higher pressure fluctuation than predicted by ADT. Once again, all the permissible non-plane modes are below cut off and hence we observe an exponential decay upstream of the stator vane for all the non-plane modes, which is in agreement with the ADT. However, the plane-mode values are dependent on the incoming temporal frequency whereas ADT predicts no such dependence. In general, it is observed that downstream pressure fluctuation spectrum predicted by ADT matches better with DNS results than upstream predictions.

Table 3.5: Comparison of upstream plane-mode values

Run	Frequency (Hz)	DNS value	ADT prediction
pw1	1000	0.017	0.016
pw2	700	0.021	0.016
pw3	400	0.019	0.016
pw4	1100	0.019	0.016

To further investigate the predictions of ADT against the DNS data, consider how well does ADT predict the decay rates of azimuthal modes which are below cut-off. The comparison has been performed at upstream and downstream stations for both the left moving waves and right moving

Table 3.6: Comparison of downstream plane-mode values

Run	Frequency (Hz)	DNS value	ADT prediction
pw1	1000	0.011	0.014
pw2	700	0.017	0.014
pw3	400	0.011	0.014
pw4	1100	0.012	0.014

waves. However, the results presented here are corresponding to the right moving waves; the left moving waves follow a similar trend. From the actuator disk theory we know that the imaginary part of complex-valued axial wavenumber leads to exponential decay of modes which have subsonic phase velocity with respect to the medium. The imaginary part of axial wavenumber depends on the azimuthal wavelength and hence different azimuthal wavelengths will have different decay rates. DNS data at the upstream and downstream stations, shown in the figure 3.5, is used to calculate the decay rate for the various azimuthal modes. The ratio of measured and predicted decay rates, $\frac{k^2_{x_{DNS}}}{k^2_{x_{ADT}}}$, for different azimuthal modes of upstream and downstream traveling waves is shown in the figures 3.10(a) and 3.10(b). It is observed that the decay rate predictions by ADT match well with DNS results for larger fY/a values, specially for the lower temporal frequencies. Upstream of the blade best correlation is observed for 400 Hz wave, whereas downstream of it best correlation is observed for 700 Hz wave. The comparison between the measured and predicted decay rates gets worse as we go to smaller and smaller fY/a.

As we discussed in chapter 2, actuator disk theory neglects the details of the blade and hence any flow gradient along the blade. It replaces the blade with a discontinuity at axial station x_0. In the remaining thesis we will address this point x_0 as origin of noise source. To investigate the validity of this assumption we used DNS data to find out the origin of noise source and its dependence on temporal frequency and spatial wavelength. The location of the noise source is found using the measured decay rate and pressure fluctuation amplitude and comparing it with the pressure

fluctuation amplitude predicted by ADT at the origin. The upstream and downstream traveling waves have been studied separately and corresponding results are shown in the figures 3.11(a) and 3.11(b), respectively. These figures show the distance of perceived origin from the trailing and leading edges of the blade for downstream and upstream traveling waves, respectively. These comparisons reveal that location of perceived noise source is different for different fY/a. Modes with smallest wavelengths exhibit strong dependence of origin on the wavelength and have their origins spread over the entire chord length for both upstream and downstream waves. However, as fY/a increases the dependence of perceived origin on the wavelength weakens as leading and trailing edges of the blade emerge out as the origin of noise source. Based on these observations, for upstream calculations we have fixed x_0 at the leading edge whereas for the downstream calculations trailing edge is found to be a better suited location for origin of the noise source. Thus, it can be concluded that changes in flow conditions throughout the chord can not be ignored completely as local acceleration of the entropy wave does contribute to the pressure fluctuations observed, however the major contribution of these pressure fluctuations comes from the trailing and leading edges.

3.5 Figures of chapter 3

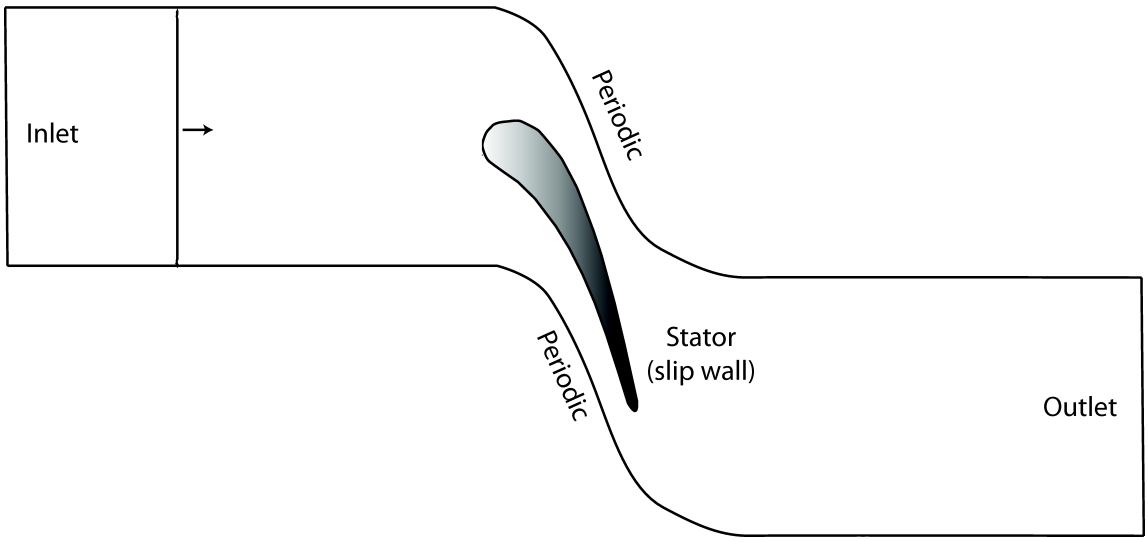

Figure 3.1: Computational domain and boundary conditions.

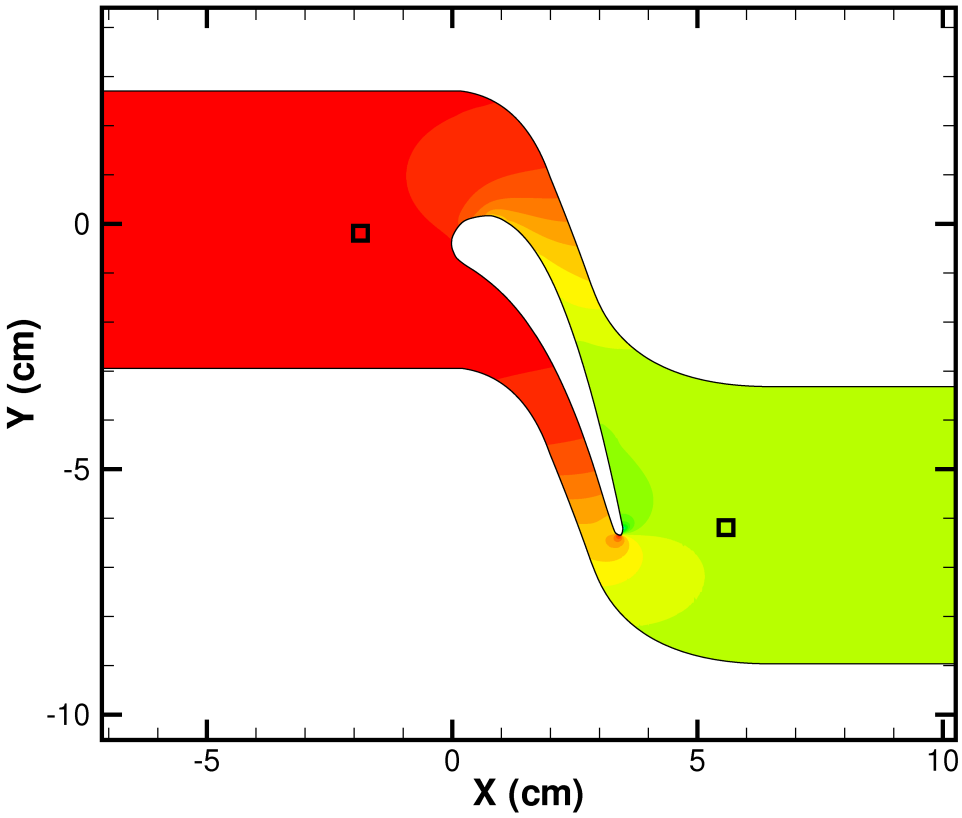

Figure 3.2: Contours of density ρ_0 representing the mean flow over stator vane. Square boxes represent probes near leading and trailing edges. Contour range from $0.5\rho_\infty$ to $\rho_i nfty$

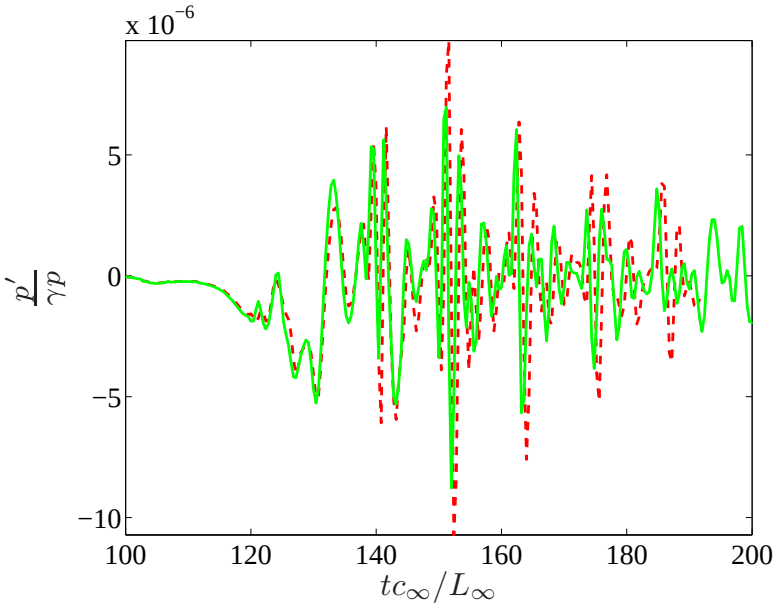

(a) Upstream

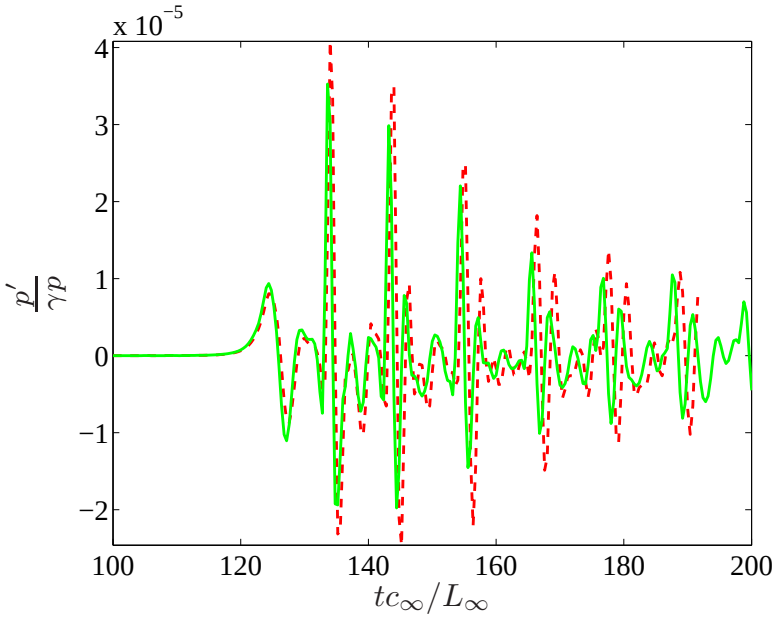

(b) Downstream

Figure 3.3: Grid converged mean flow: comparison between pressure fluctuations for grids with 0.3 M and 1.2 M grid points at upstream and downstream probe stations. Legend: −− 0.3 M and — 1.2 M.

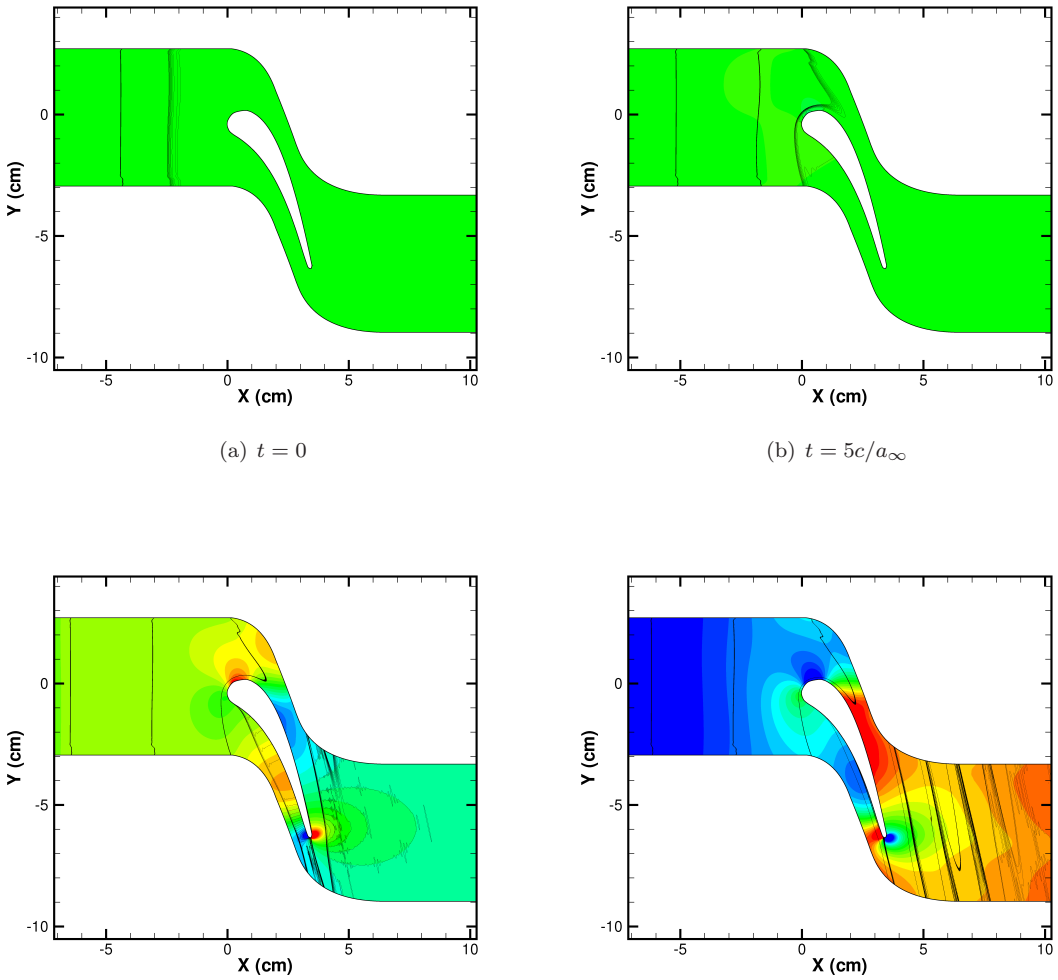

(a) $t = 0$

(b) $t = 5c/a_\infty$

(c) $t = 10c/a_\infty$

(d) $t = 15c/a_\infty$

Figure 3.4: Four consecutive instantaneous views of the density disturbance (solid lines) and pressure disturbance (contours) corresponding to test case pw1. Time increases from left to right. Density contour lines of $|\rho'| \leq 1.0 \times 10^{-3}\rho_\infty$ and pressure contours of $|P'| \leq 1.5 \times 10^{-3}P_\infty$ are shown.

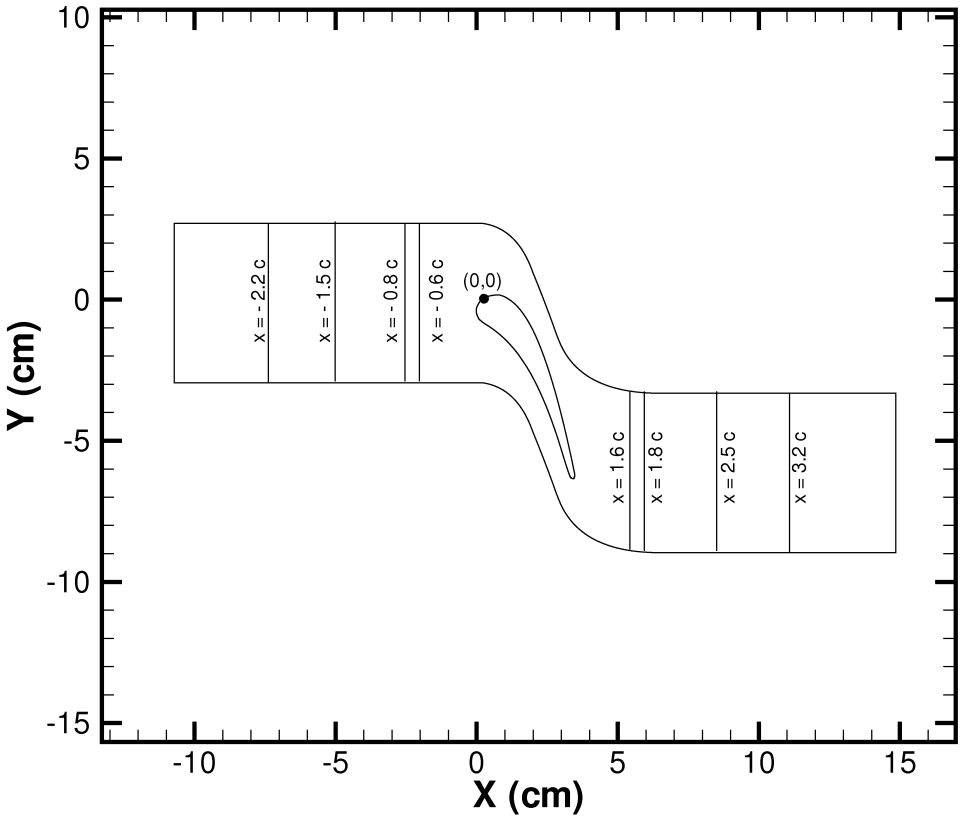

Figure 3.5: Probe stations for evaluation of DNS results.

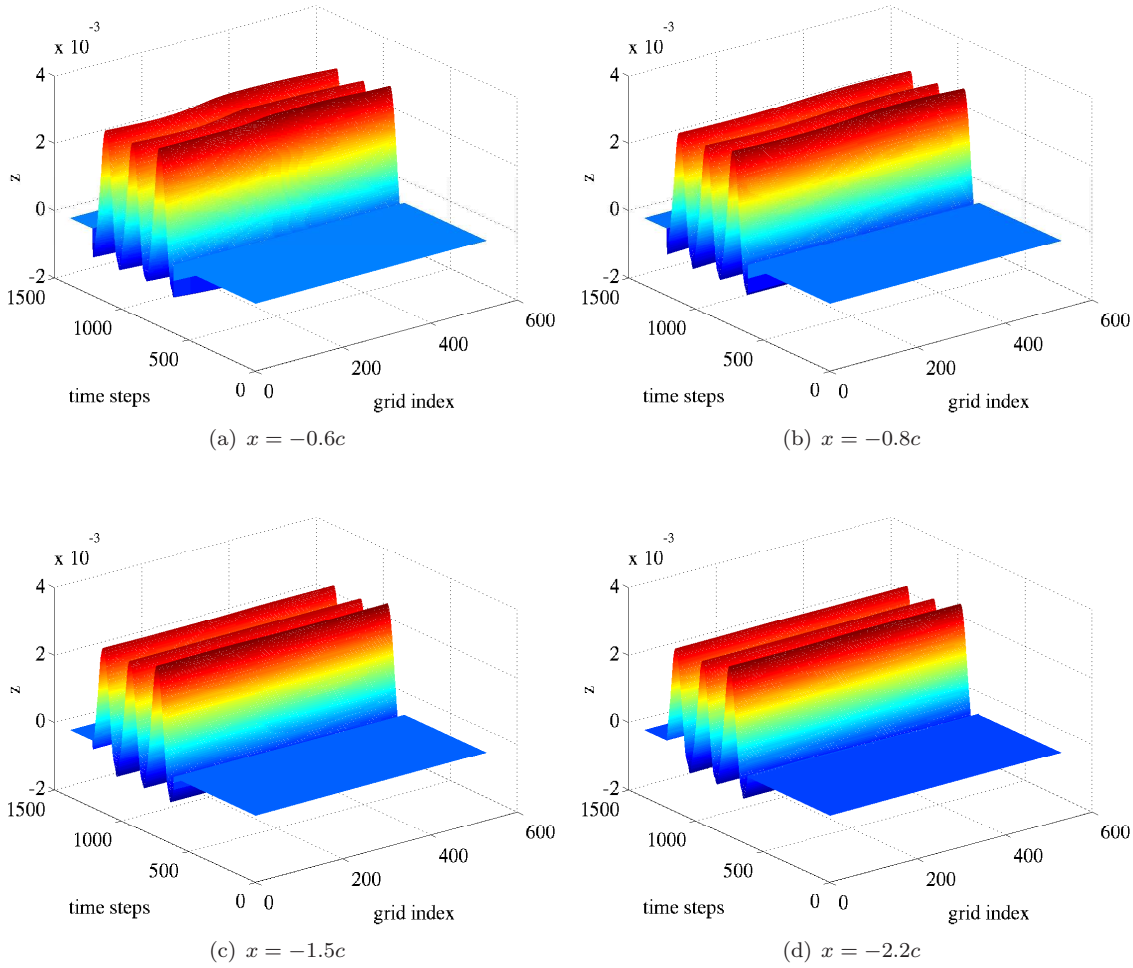

(a) $x = -0.6c$ (b) $x = -0.8c$

(c) $x = -1.5c$ (d) $x = -2.2c$

Figure 3.6: 3-dimensional representation of azimuthal and temporal variation of pressure fluctuations at various upstream probe stations.The z-label is $|p'/\gamma p|$

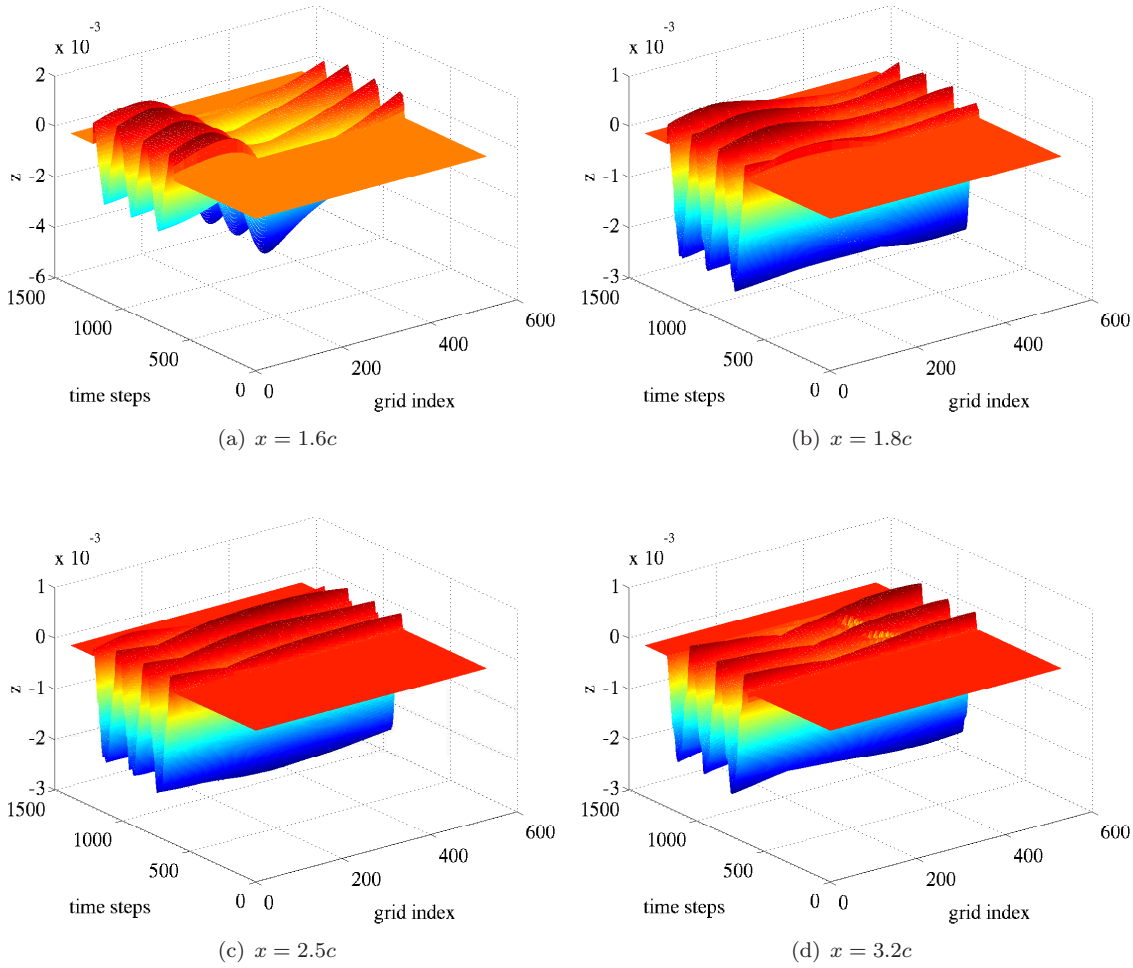

(a) $x = 1.6c$ (b) $x = 1.8c$

(c) $x = 2.5c$ (d) $x = 3.2c$

Figure 3.7: 3-dimensional representation of azimuthal and temporal variation of pressure fluctuations at various downstream probe stations. The z-label is $|p'/\gamma p|$

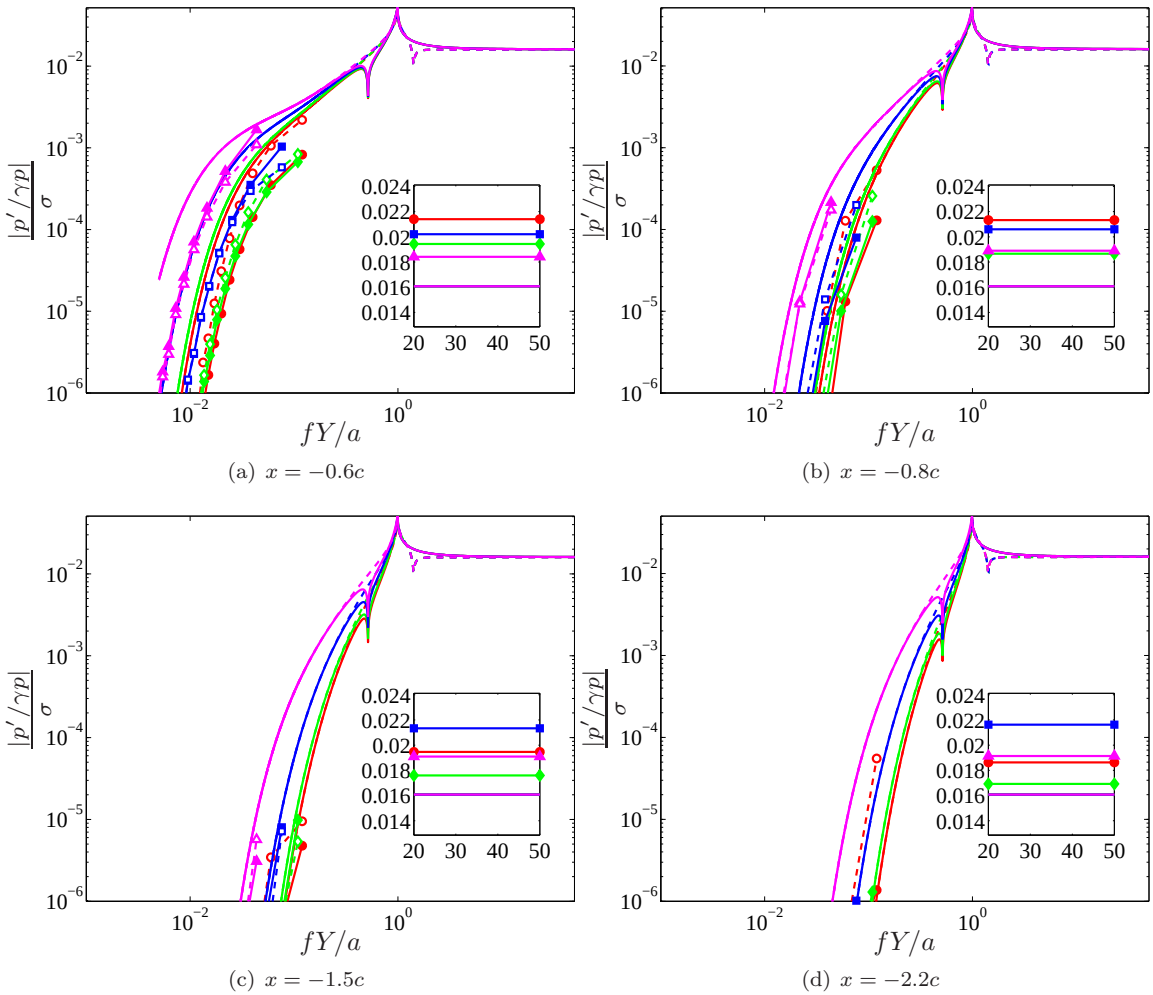

(a) $x = -0.6c$ (b) $x = -0.8c$

(c) $x = -1.5c$ (d) $x = -2.2c$

Figure 3.8: Comparison between pressure fluctuation magnitude of ADT and DNS results at upstream probe stations for incoming plane waves of 1000 Hz, 700 Hz, 400 Hz and non-planar wave of 1100 Hz. Legend: — ADT prediction for right moving wave, 400 Hz; ▲ DNS result for right moving wave, 400 Hz; – – – ADT prediction for left moving wave, 400 Hz; △ DNS result for left moving wave, 400 Hz; — ADT prediction for right moving wave, 700 Hz; ■ DNS result for right moving wave, 700 Hz; – – – ADT prediction for left moving wave, 700 Hz; □ DNS result for left moving wave, 700 Hz; — ADT prediction for right moving wave, 1000 Hz; ♦ DNS result for right moving wave, 1000 Hz; – – – ADT prediction for left moving wave, 1000 Hz; ◇ DNS result for left moving wave, 1000 Hz; — ADT prediction for right moving wave, 1100 Hz; ● DNS result for right moving wave, 1100 Hz; – – – ADT prediction for left moving wave, 1100 Hz; ○ DNS result for left moving wave, 1100 Hz.

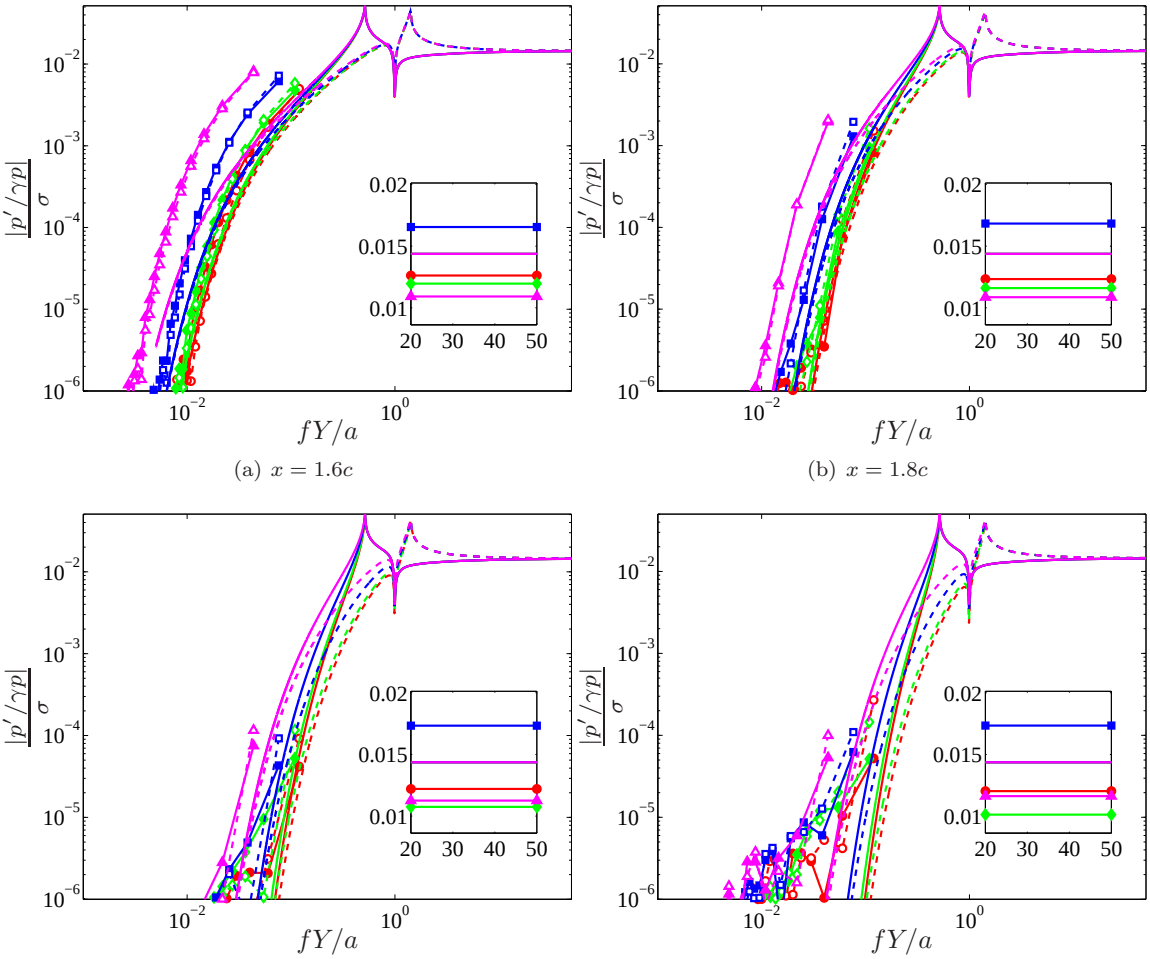

(a) $x = 1.6c$ (b) $x = 1.8c$

(c) $x = 2.5c$ (d) $x = 3.2c$

Figure 3.9: Comparison between pressure fluctuation magnitude of ADT and DNS results at downstream probe stations for incoming plane waves of 1000 Hz, 700 Hz, 400 Hz and non-planar wave of 1100 Hz. Legend: — ADT prediction for right moving wave, 400 Hz; ▲ DNS result for right moving wave, 400 Hz; – – – ADT prediction for left moving wave, 400 Hz; △ DNS result for left moving wave, 400 Hz; — ADT prediction for right moving wave, 700 Hz; ■ DNS result for right moving wave, 700 Hz; – – – ADT prediction for left moving wave, 700 Hz; □ DNS result for left moving wave, 700 Hz; — ADT prediction for right moving wave, 1000 Hz; ♦ DNS result for right moving wave, 1000 Hz; – – – ADT prediction for left moving wave, 1000 Hz; ◇ DNS result for left moving wave, 1000 Hz; — ADT prediction for right moving wave, 1100 Hz; ● DNS result for right moving wave, 1100 Hz; – – – ADT prediction for left moving wave, 1100 Hz; ○ DNS result for left moving wave, 1100 Hz. Inset figures show the plane azimuthal mode corresponding to different cases.

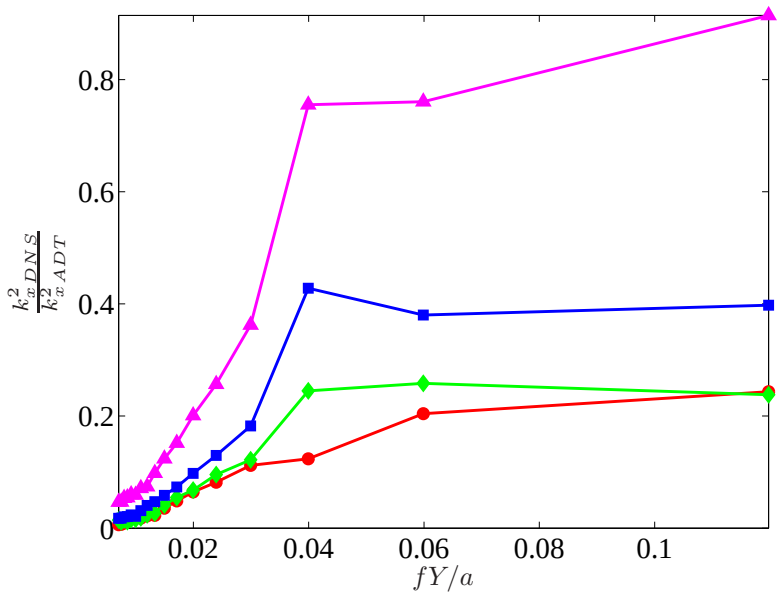

(a) Upstream

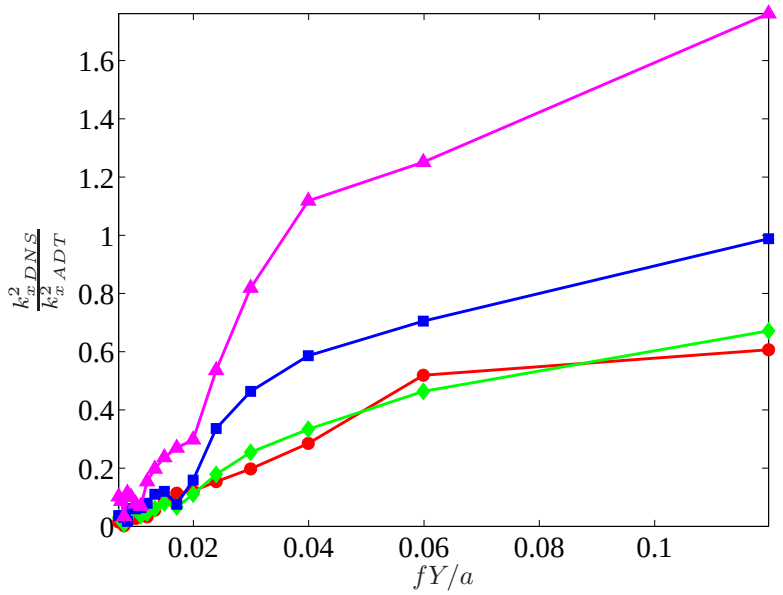

(b) Downstream

Figure 3.10: Comparison of axial decay rate between the DNS results and ADT predictions. Legend: ▲ right moving wave, 400 Hz; ■ right moving wave, 700 Hz; ♦ right moving wave, 1000 Hz; ● right moving wave, 1100 Hz;

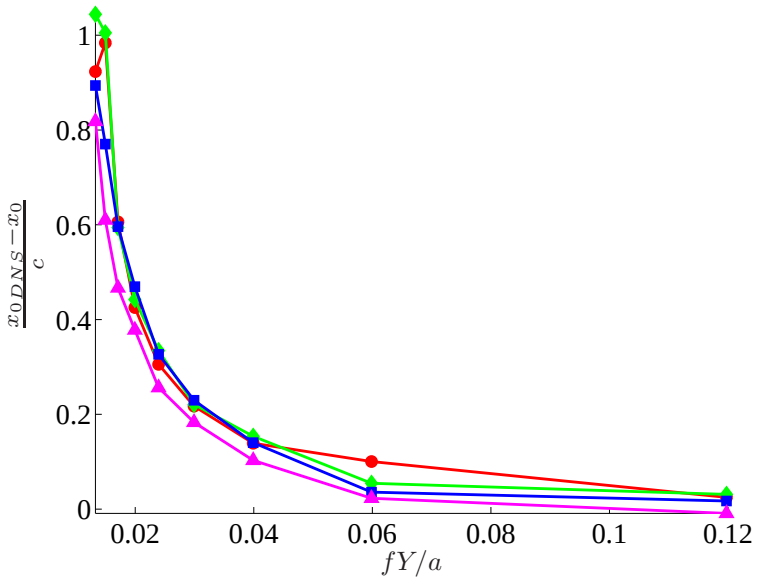

(a) Upstream

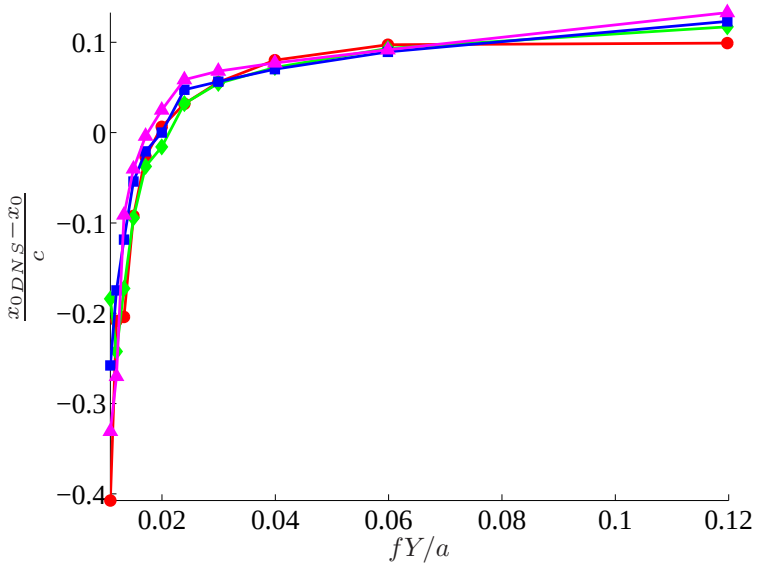

(b) Downstream

Figure 3.11: Location of perceived noise source in DNS results and its relative distance from leading and trailing edges for upstream and downstream waves. $x_0 = x_L E$ for upstream and $x_0 = x_T E$ for downstream. Legend: ▲ right moving wave, 400 Hz; ■ right moving wave, 700 Hz; ♦ right moving wave, 1000 Hz; ● right moving wave, 1100 Hz;

Chapter 4

Direct numerical simulation of localized entropy disturbance

Apart from validating the actuator disk results for a low-frequency plane-wave entropic disturbances, we also carried out direct numerical simulation for localized, high frequency entropy pulses. The level of entropy disturbance was taken to be similar to that found in real engines as documented in a report for a Pratt and Whitney JT8D-9 engine by Cumpsty and Marble [22]. The root-mean-square entropy level was roughly $s'/c_p = 0.02$ with a simple Gaussian distribution of

$$\frac{s'}{c_p} = \ln\left\{1 + \frac{T'}{T_\infty}\right\} \tag{4.1}$$

where $T'/T_\infty = A\exp\{-(x-x_i)^2/L_x^2 - (y-y_i)^2/L_y^2\}$. The amplitude A and initial vertical location y_i (see figure 4.1) for an asymmetric blade are varied according to the values in table 4.1. The initial axial location x_i governs the time at which entropy disturbance interacts with the turbine blade and does not affect results, so long as x_i is chosen sufficiently upstream of the leading edge. For the current procedure the fixed value of $x_i = -0.5b$, where b is the inter-blade spacing, was chosen as a compromise between being placed in the far upstream where the flow is more uniform but the grid is not sufficiently refined and being placed too close to the airfoil where the flow is not uniform.

To demonstrate a sample interaction, consider a particular disturbance case, hs1, from table 4.1. Let $\rho_0(x)$ be the steady state density field. Then define the difference between the current density and its steady-state value, $\rho' = \rho - \rho_0$. Let $p_0(x)$ be the steady state pressure field. Then define the difference between the current pressure and its steady-state value, $p' = p - p_0$. This report uses these two difference quantities to analyze the results obtained for the CERTS stator.

Table 4.1: Parameters for direct simulation: Localized entropy pulse.

Run	A	y_0/b	L_x/b	L_y/b	M_∞
hs1	0.025	0.0	0.015	0.015	0.10
hs2	0.025	0.17	0.015	0.015	0.10
hs3	0.025	0.35	0.015	0.015	0.10
hs4	0.025	-0.17	0.015	0.015	0.10
hs5	0.025	-0.35	0.015	0.015	0.10
hs6	0.005	0.0	0.015	0.015	0.10
hs7	0.035	0.0	0.015	0.015	0.10

The entropy disturbance is stretched by the highly-nonuniform mean flow and creates, among other things, local pockets of reduced momentum. These momentum deficits are accompanied by a non-uniform pressure field which has support over a larger region. When the pressure disturbance field associated with the entropy disturbance interacts with the blade's trailing edge, it is scattered into sound. It has been observed that first local maxima of pressure perturbations occur when the entropy pulse is near the trailing edge. A time sequence of four views of the density disturbance $\rho - \rho_0$ (as isolines) and disturbance pressure $p - p_0$ (as contours) is shown in figure 4.2. Similarly, figure 4.3 shows the results corresponding to test case hs4. In this test case pulse hits the blade head on and faces maximum effect of upstream stagnation point. The results of the other test cases have not been presented here.

To analyze the effect of amplitude of entropy fluctuations on the resulting pressure fluctuations, different amplitudes (hs1, hs6 and hs7) were considered. It is found that behavior is linear with respect to the amplitude for the cases considered, figure 4.4. To study the effect of initial vertical location y_i on pressure fluctuation amplitude, the test cases whose amplitude of entropy pulse is same, cases hs1 $-$ hs5, are compared. The pressure fluctuation amplitude at the probe stations near

the leading and trailing edges shows that test case hs1 produces maximum pressure fluctuations near the blade. In this test case, the entropy pulse convects with the mean flow and just grazes over the suction surface of the stator vane. Pressure disturbance variations with time are given in figure 4.5 and figure 4.6 for the two probe locations shown in figure 3.2, respectively. However, this observation does not hold true for probe stations far from the blade because the cut-off azimuthal modes which are dominant near the blade, decay exponentially both upstream and downstream of the blade. Hence, to compare which test case produces maximum pressure fluctuations in the far field, it is important to compare pressure-fluctuations of non-evanescent modes. Thus, to further investigate the dependence of pressure fluctuation amplitude on initial vertical location of pulse in the far-field, the two dimensional Fourier transform in time and azimuthal direction was taken and comparison between the plane-mode pressure fluctuation amplitude is performed for test cases hs1 − hs5. The corresponding results are shown in the figures 4.7(a) and 4.7(b). It is observed that upstream far-field of the blade test case hs1 produces maximum pressure fluctuation whereas downstream far-field observes maximum pressure fluctuation in the test case hs4. The entropy pulse goes through maximum non-uniformity in these two test cases for, e.g., in the test case hs4 the entropy pulse collides head on with the blade's leading edge and bears the maximum effect of upstream stagnation point and thus produces large pressure fluctuations downstream of the blade. Whereas, in the test case hs1 the entropy pulse just grazes over the suction surface and goes through maximum acceleration among all the test cases and produces maximum pressure fluctuation upstream of the blade.

4.1 Comparison of DNS results with ADT

DNS results of the test cases presented in table 4.1 for the operating condition given in table 3.2 are compared against those predicted by the actuator disk theory for an isolated blade row of CERTS stator vane. The upstream and downstream conditions used in ADT calculations are given in table 4.2. Upstream and downstream flow Mach numbers and flow directions have been obtained by taking average of the corresponding values obtained at all the upstream and downstream probe

stations, shown in figure 3.5, respectively.

Table 4.2: Upstream and downstream flow parameters for ADT

location	M	θ (deg)
Upstream	0.10	0
Downstream	0.59	-78.03

Two dimensional Fourier transform of periodic pressure signal is calculated in order to understand the temporal and azimuthal spectra of the pressure fluctuations. Fourier representation of the pressure waves shows that temporal spectra of the pulse comprises of waves of frequencies higher than $5000Hz$. The first three modes correspond to 5088 Hz, 10064 Hz and 15160 Hz.

Comparisons have been made at various upstream and downstream probe stations for entropy pulses of test cases hs1 − hs8. These probe locations have been used to compare DNS and ADT results. Results shown in figures 4.8 and 4.9 correspond to 5088 Hz temporal frequency of the entropy pulse case hs1. First, consider the downstream results starting with the nearest probe station from the blade. It is observed that the pressure amplitudes obtained by DNS are higher than those predicted by ADT for all the wavelengths including the plane mode, $k_y = 0$. The upstream and downstream plane mode values are given in the tables 4.3 and 4.4, respectively. Similar trends are observed at all the other downstream locations. Upstream pressure fluctuation amplitudes are also seen to be deviating from those predicted by ADT and invariably have higher amplitude than predicted by ADT.

To further investigate the predictions of ADT against the DNS data, the ADT-predicted decay rates of azimuthal modes which are below cut-off for a high-frequency localized pulse are also presented. The comparison has been performed at upstream and downstream stations for both the left moving waves and right moving waves. However, the results presented here are corresponding to the right moving waves, the left moving waves follow a similar trend. From the actuator disk theory we know that the imaginary part of the complex-valued axial wavenumber leads to exponential decay

of modes which have subsonic phase velocity with respect to the medium. The imaginary part of axial wavenumber depends on the azimuthal wavelength and, hence, different azimuthal wavelengths will have different decay rates. The DNS data at the upstream and downstream stations, shown in the figure 3.5, is used to calculate the decay rate for the various azimuthal modes. The ratio of measured and predicted decay rates, $\frac{k^2_{x_{DNS}}}{k^2_{x_{ADT}}}$, for different azimuthal modes of upstream and downstream traveling waves is shown in the figures 4.10(a) and 4.10(b). Unlike low-frequency plane-waves, we see that the measured decay rates from DNS data are an order of magnitude lower than predicted by ADT and the matching between DNS results and ADT predictions is not at all satisfactory at these higher frequencies.

As we found out in chapter 2, actuator disk theory neglects the details of the blade and hence any flow gradient along the blade. It replaces the blade with a discontinuity at axial station x_0. We address this point x_0 as origin of noise source. To investigate the validity of this assumption we used DNS data to find out the origin of noise source and its dependence on temporal frequency and spatial wavelength. The location of noise source is found using the measured decay rate and pressure fluctuation amplitude and comparing it with the pressure fluctuation amplitude predicted by ADT at the origin. The upstream and downstream traveling waves have been studied separately and corresponding results are shown in the figures 4.11(a) and 4.11(b), respectively. These figures show the distance of perceived origin from the trailing and leading edges of the blade for downstream and upstream traveling waves, respectively. These comparisons reveal that location of perceived noise source is different for different wavelengths. Just like what we observed for low-frequency waves, modes with smallest values of fY/a exhibit strong dependence of origin on the wavelength and have their origins spread over the entire chord length for both upstream and downstream waves. However, unlike what we observed for low-frequency waves that for higher wavelengths location of noise source have weaker dependence on wavelength and leading and trailing edge appear to be noise source for larger values of fY/a, for localized pulse we see that there is no such trend that can be observed for higher wavelengths and location of noise source varies with wavelengths for all the modes. These observations show us that in case of a high frequency concentrated pulse, ADT predictions are not as close to DNS results as in the case of low-frequency planar waves, which

is because at higher frequencies the spacial wavelength is not large enough for compact source assumption to be valid, which is one of the key assumptions of ADT.

Table 4.3: Comparison of upstream plane-mode values

Run	Frequency (Hz)	DNS	ADT
hs1	5088	0.041	0.018
hs1	10064	0.045	0.018
hs1	15160	0.048	0.018

Table 4.4: Comparison of downstream plane-mode values

Run	Frequency (Hz)	DNS	ADT
hs1	5088	0.023	0.018
hs1	10064	0.026	0.018
hs1	15160	0.028	0.018

4.2 Comparison with low frequency planar wave

Another set of simulations was carried out with plane-wave entropic disturbance in the free stream. However, it was simulated for the same flow conditions as those for localized pulse in the previous section. These flow parameters are specified in table 3.2. The temporal frequency of incoming entropy wave for these simulations has been chosen to be 1000 Hz. A time sequence of four views of the density disturbance $\rho - \rho_0$ (as isolines) and disturbance pressure $p - p_0$ (as contours), is shown in figure 4.12.

The resulting pressure perturbation at upstream and downstream probe stations, figure 3.5, is captured in 3-dimensional plots which depict the temporal and azimuthal wave nature of pressure

perturbations. For illustrative purposes, 3-D plots are shown in figures 4.13 and 4.14. It is observed that the pressure waves lose their azimuthal variation and become more and more planar as they move farther and father upstream and downstream of the blade.

Comparison between upstream and downstream ADT predictions and DNS results is shown in figures 4.15 and 4.16, respectively. The upstream and downstream conditions used in ADT calculations are given in table 4.2. It is observed that DNS results are in close agreement with ADT predictions, both upstream and downstream of the blade. The upstream and downstream plane mode values obtained by DNS and ADT are given in the tables 4.5. It is observed that the agreement between DNS and ADT results for a low frequency plane wave is much better than that of high frequency localized pulse, for the same operating conditions. To further verify ADT predictions, a comparison has been performed between the decay rates predicted by ADT and those obtained using DNS data at upstream and downstream stations for both the left moving waves and right moving waves. However, the results presented here are corresponding to the right moving waves, the left moving waves follow a similar trend. DNS data at the upstream and downstream stations, shown in the figure 3.5, is used to calculate the decay rate for the various azimuthal modes. The ratio of measured and predicted decay rates, $\frac{k^2_{x_{DNS}}}{k^2_{x_{ADT}}}$, for different azimuthal modes of upstream and downstream traveling waves is shown in the figures 4.17(a) and 4.17(b). We observe that for these low-frequency waves ADT predictions are in agreement with the DNS results, specially at the azimuthal modes having higher wavelength. Thus ADT prediction for decay of evanescent modes, in the same operating conditions, is much better for a low-frequency plane-wave entropic disturbance than a high-frequency localized pulse.

To verify the assumption of ADT to ignore the details of the blade and replace it with a discontinuity at a position x_0, we used DNS data to find out the origin of perceived noise source and its dependence on temporal frequency and spatial wavelength. The location of noise source is found using the measured decay rate and pressure fluctuation amplitude and comparing it with the pressure fluctuation amplitude predicted by ADT at the origin. The upstream and downstream traveling waves have been studied separately and corresponding results are shown in the figures 4.18(a) and 4.18(b), respectively. These figures show the distance of perceived origin from the trailing and

leading edges of the blade for downstream and upstream traveling waves, respectively. These comparisons reveal that location of perceived noise source is different for different wavelengths. Modes with smallest values of fY/a exhibit strong dependence of origin on the wavelength and have their origins spread over the entire chord length for both upstream and downstream waves. However, as fY/a increases the dependence of perceived origin on the wavelength weakens as leading and trailing edges of the blade emerge out as the origin of noise source. Based on these observations, for upstream calculations we have fixed x_0 at the leading edge whereas for the downstream calculations trailing edge is found to be a better suited location for origin of the noise source. Thus, it can be concluded that changes in flow conditions throughout the chord can not be ignored completely as local acceleration of the entropy wave does contribute to the pressure fluctuations observed, however major contribution of these pressure fluctuations comes from the trailing and leading edges. Thus, a reasonable prediction of pressure disturbance field due to low-frequency input entropy disturbance can be obtained using ADT by fixing x_0 at the leading and trailing edges of the blade, for upstream and downstream traveling waves respectively. However, actuator disk theory fails to predict the decay rates of evanescent modes and amplitudes of the plane-modes when the incoming entropy disturbance has high frequency. These observation again strengthens that at higher frequencies the axial wavelength is not long enough for details along the chord of the blade to be ignored and hence compact source assumption on ADT is not applicable.

Table 4.5: Comparison of plane-mode values

Location	Frequency (Hz)	DNS	ADT
Upstream	1000	0.015	0.018
Downstream	1000	0.012	0.018

4.3 Figures of chapter 4

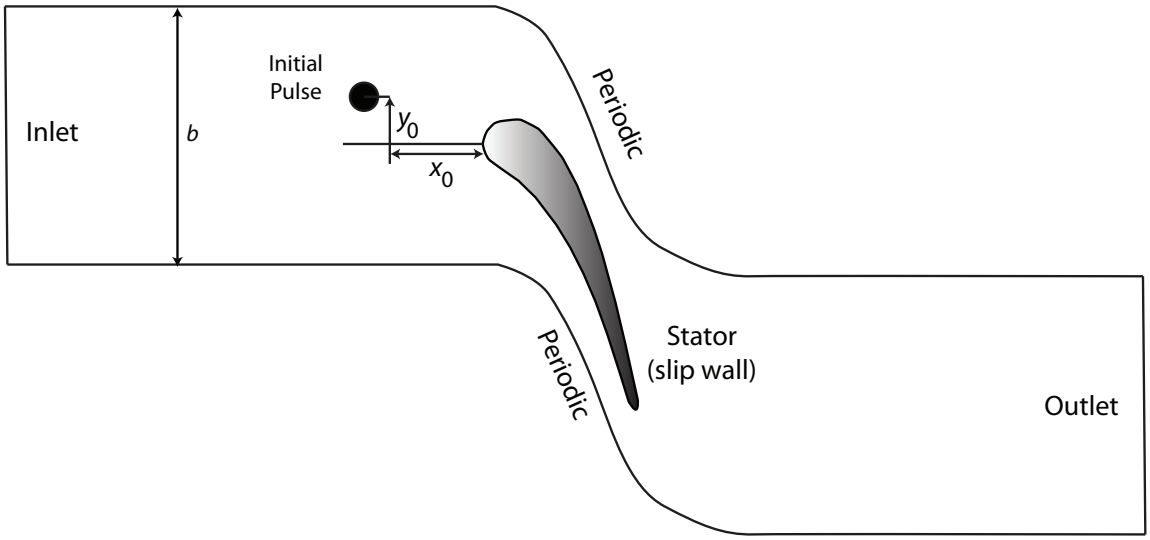

Figure 4.1: Computational domain and boundary conditions.

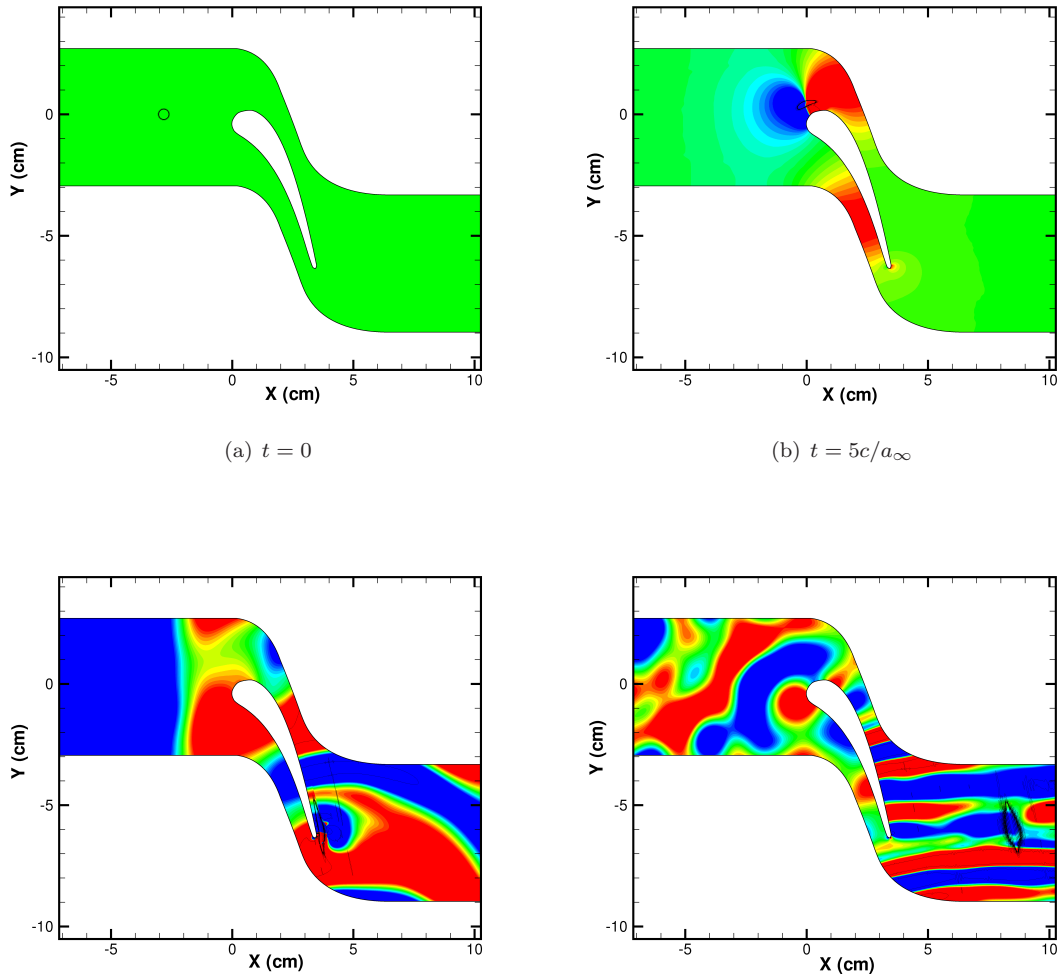

(a) $t = 0$

(b) $t = 5c/a_\infty$

(c) $t = 7c/a_\infty$

(d) $t = 15c/a_\infty$

Figure 4.2: Four consecutive instantaneous views of the density disturbance (solid lines) and pressure disturbance (contours) corresponding to test case hs1. Time increases from left to right. Density contour lines of $|\rho'| \leq 1.0 \times 10^{-4}\rho_\infty$ and pressure contours of $|P'| \leq 1.0 \times 10^{-6}P_\infty$ are shown.

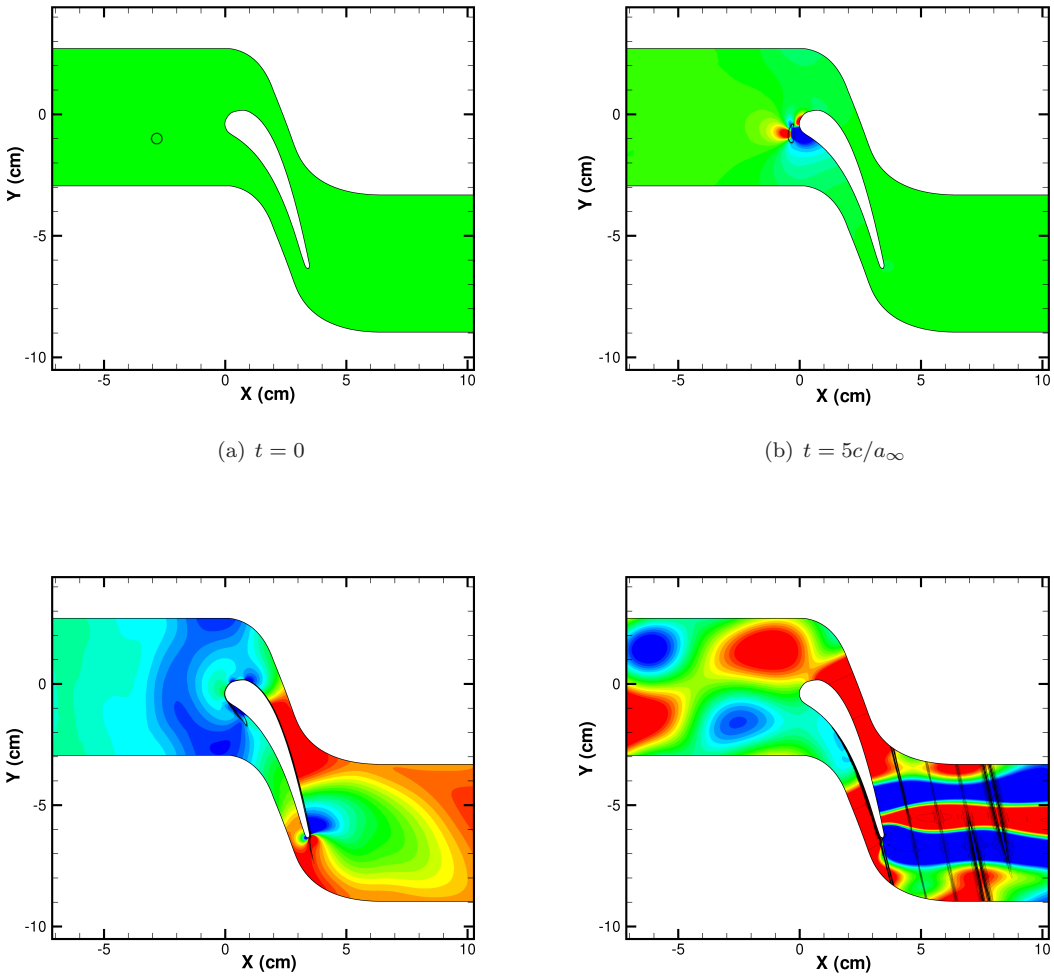

(a) $t = 0$

(b) $t = 5c/a_\infty$

(c) $t = 7c/a_\infty$

(d) $t = 15c/a_\infty$

Figure 4.3: Four consecutive instantaneous views of the density disturbance (solid lines) and pressure disturbance (contours) corresponding to test case hs4. Time increases from left to right. Density contour lines of $|\rho'| \leq 1.0 \times 10^{-4}\rho_\infty$ and pressure contours of $|P'| \leq 1.0 \times 10^{-6}P_\infty$ are shown.

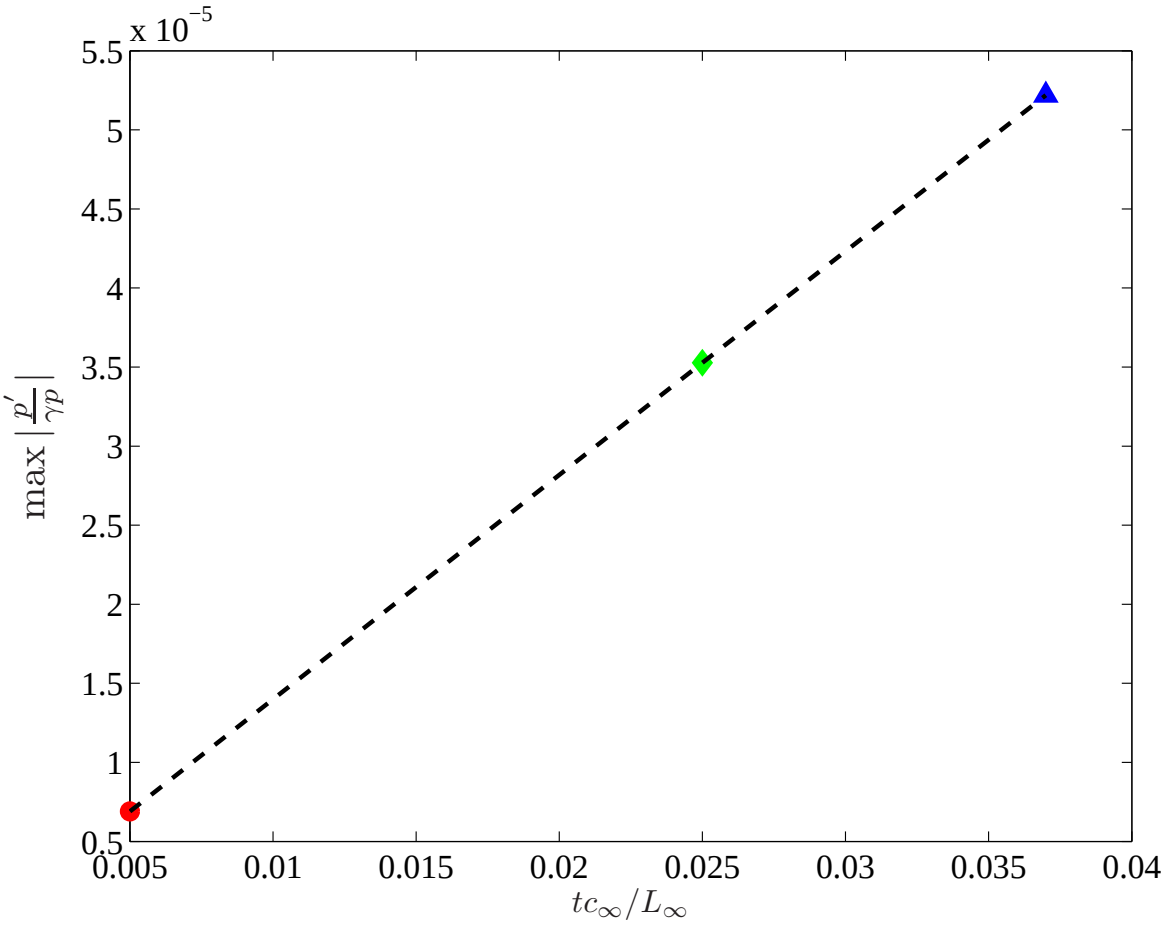

Figure 4.4: Linear dependence of pressure fluctuation on amplitude, A of incoming entropy pulse. Legend: ● hs1; ♦ hs6; ▲ hs7.

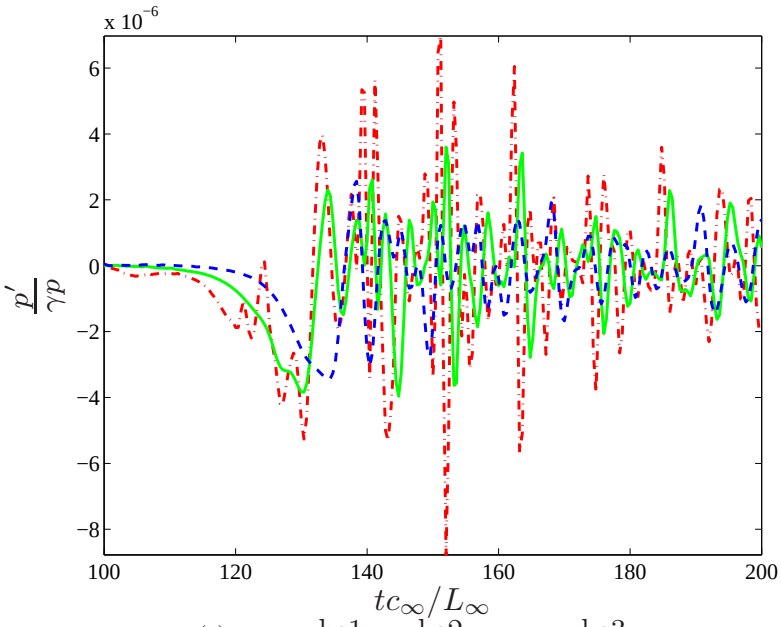

(a) — · — hs1; — hs2; — — — hs3

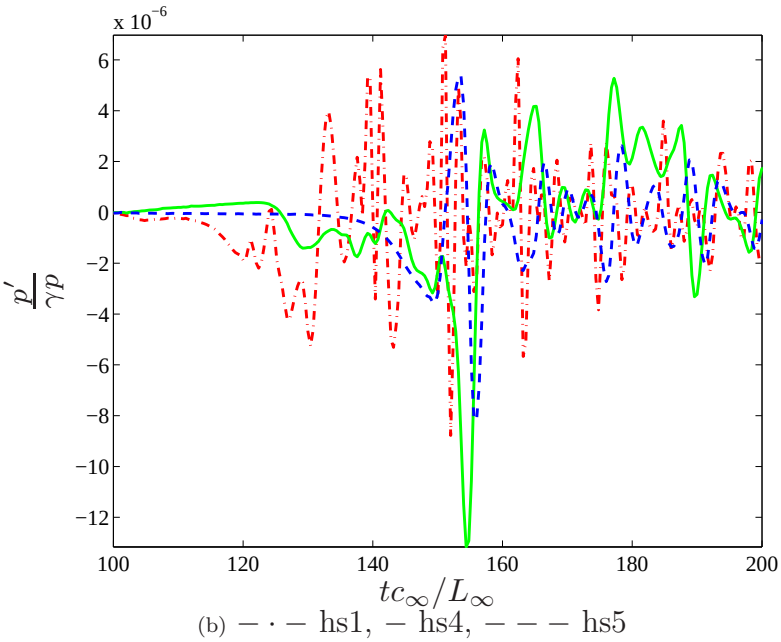

(b) — · — hs1, — hs4, — — — hs5

Figure 4.5: Variation of pressure disturbance with time at the upstream probe station near the leading edge shown in figure 3.2.

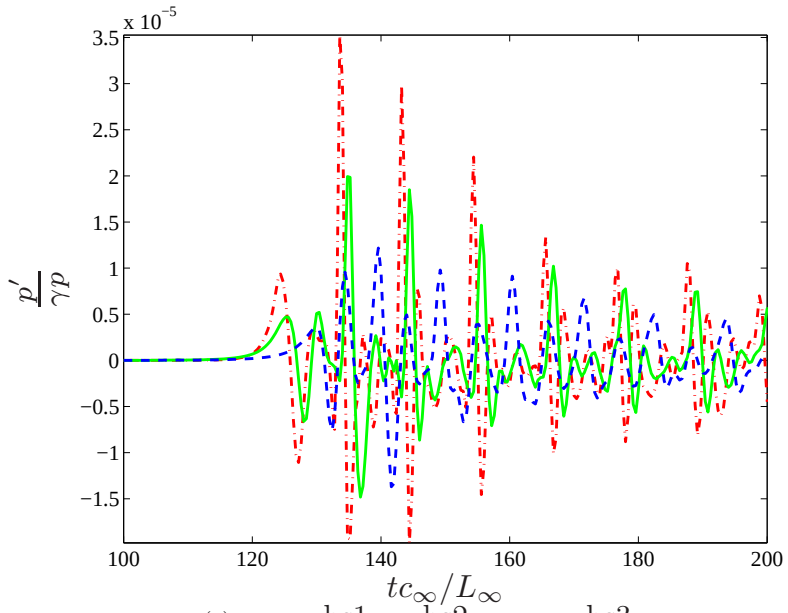

(a) — · — hs1; — hs2; — — — hs3

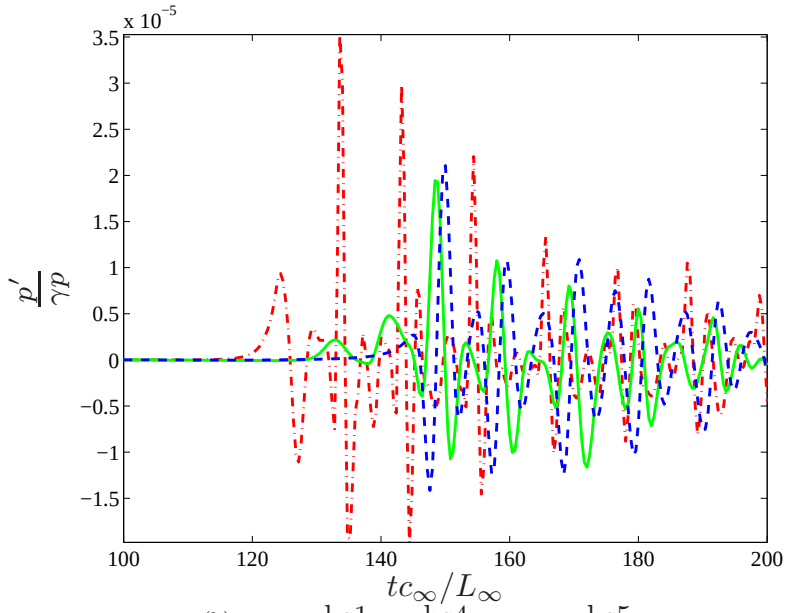

(b) — · — hs1, — hs4, — — — hs5

Figure 4.6: Variation of pressure disturbance with time at the downstream probe station near the trailing edge shown in figure 3.2.

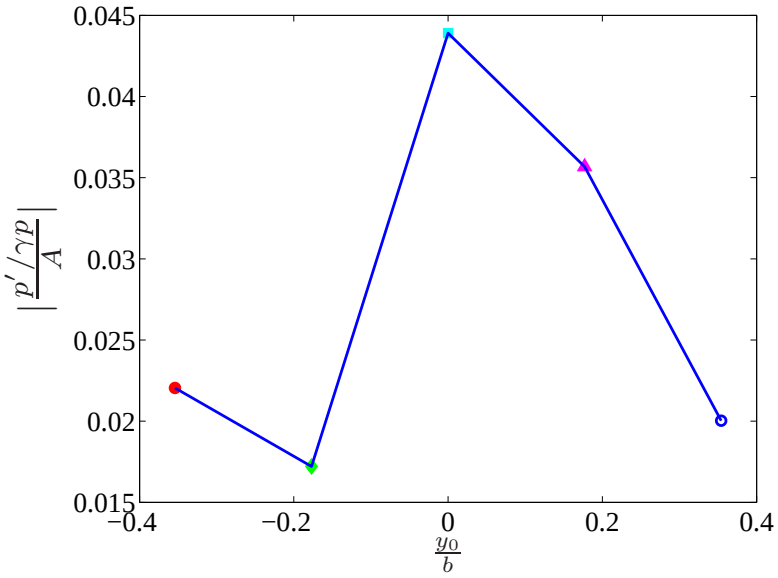

(a) Upstream

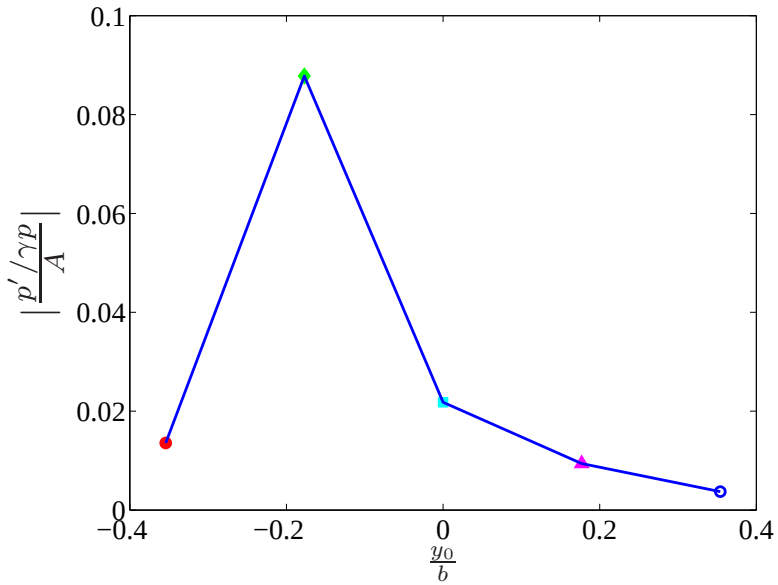

(b) Downstream

Figure 4.7: Linear dependence of pressure fluctuation on initial vertical location, y_0 of incoming entropy pulse. Legend: ■ hs1; ▲ hs2. ○ hs3; ♦ hs4; ● hs5.

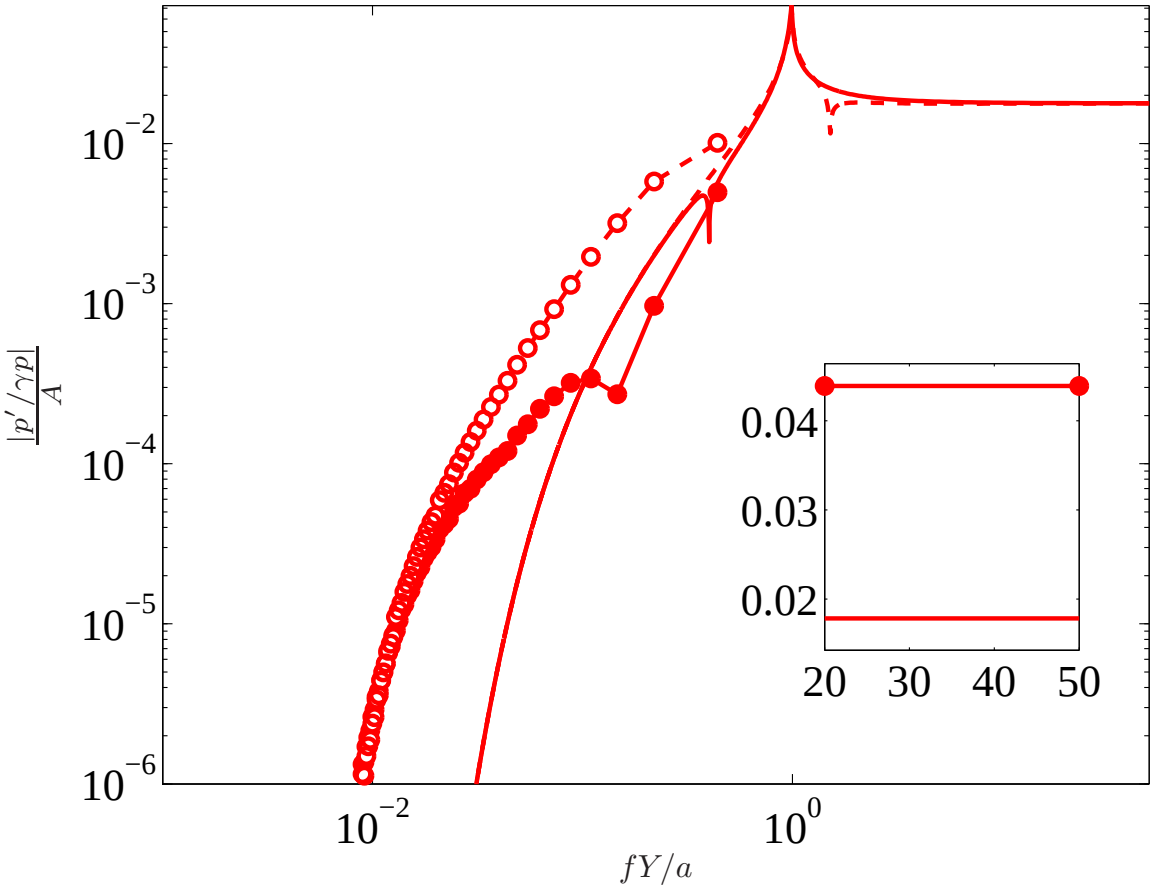

Figure 4.8: Comparison between pressure fluctuation magnitude of ADT and DNS results at the first upstream probe station. Legend: — ADT prediction for right moving wave; ● DNS result for right moving wave; – – – ADT prediction for left moving wave; ○ DNS result for left moving wave. Inset figure shows the plane azimuthal mode.

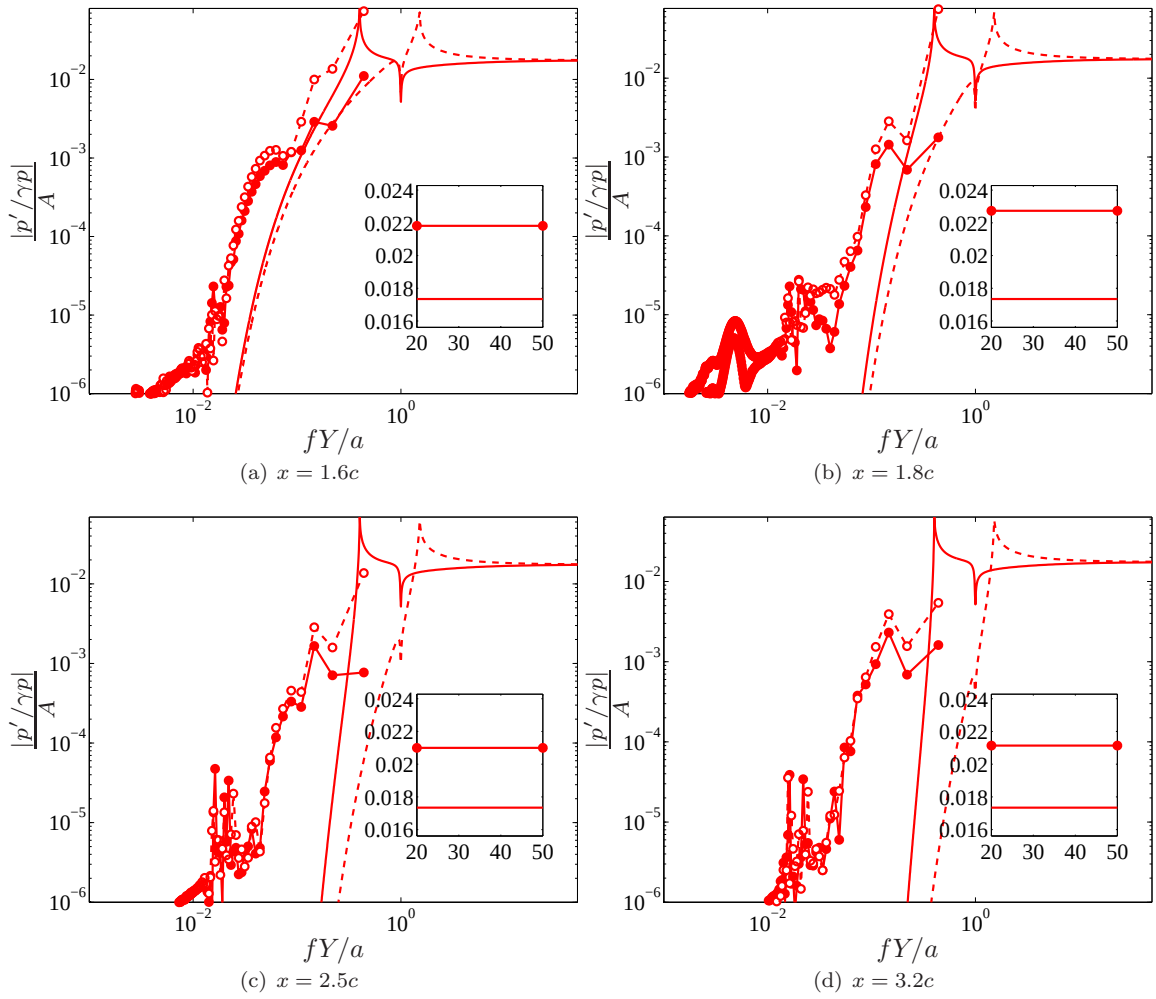

(a) $x = 1.6c$ (b) $x = 1.8c$

(c) $x = 2.5c$ (d) $x = 3.2c$

Figure 4.9: Comparison between pressure fluctuation magnitude of ADT and DNS results at the downstream probe stations. Legend: — ADT prediction for right moving wave; ● DNS result for right moving wave; – – – ADT prediction for left moving wave; ○ DNS result for left moving wave. Inset figures show the plane azimuthal mode corresponding to different cases.

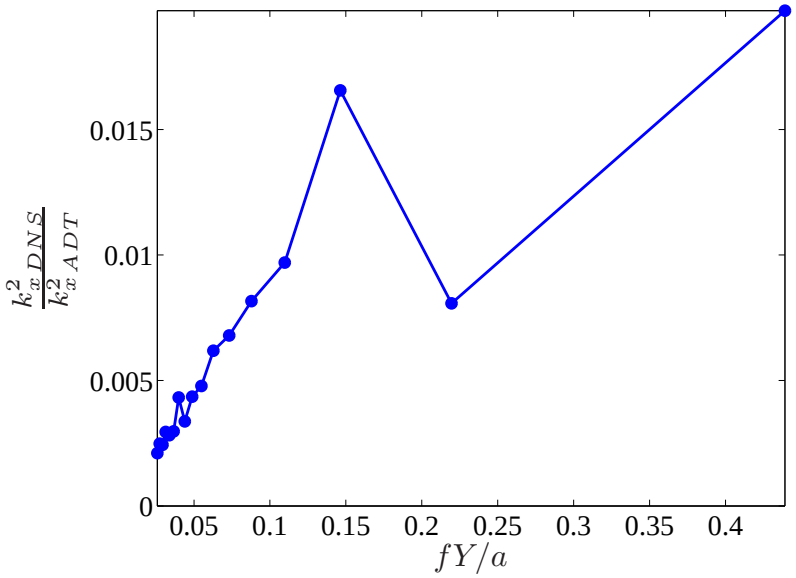

(a) Upstream

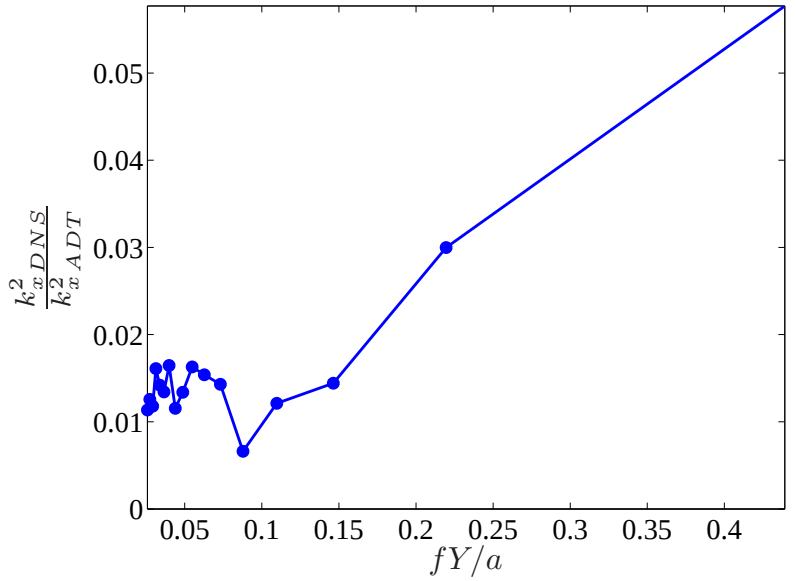

(b) Downstream

Figure 4.10: Comparison of axial decay rate between the DNS results and ADT predictions. Legend: ● right moving wave, 5088 Hz;

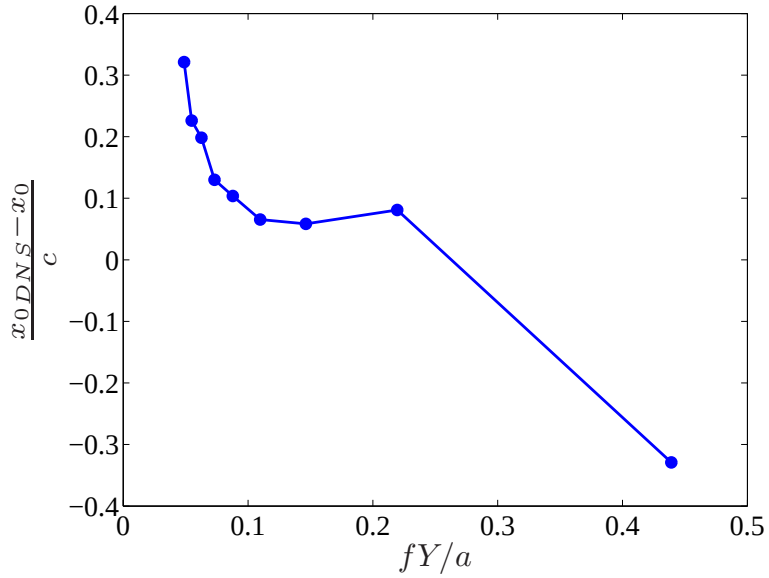

(a) Upstream

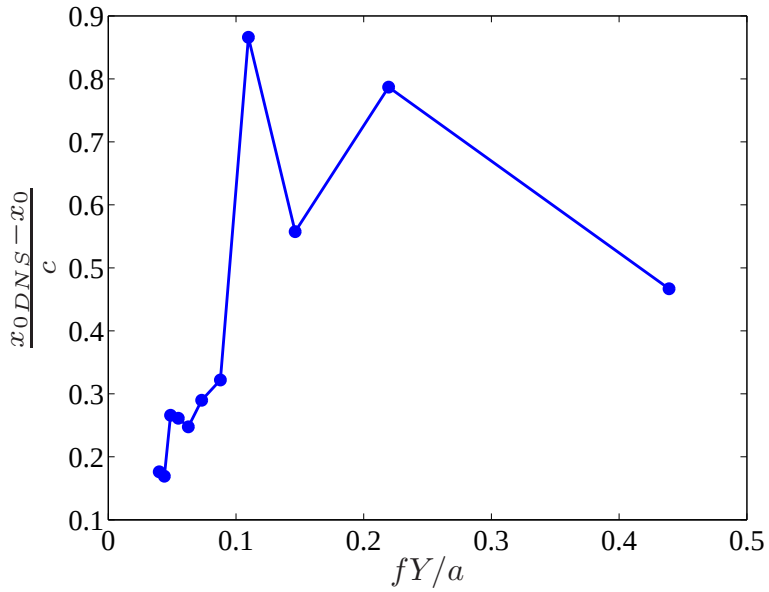

(b) Downstream

Figure 4.11: Location of perceived noise source in DNS results and its relative distance from leading and trailing edges for upstream and downstream waves. $x_0 = x_L E$ for upstream and $x_0 = x_T E$ for downstream. Legend: ● right moving wave, 5088 Hz;

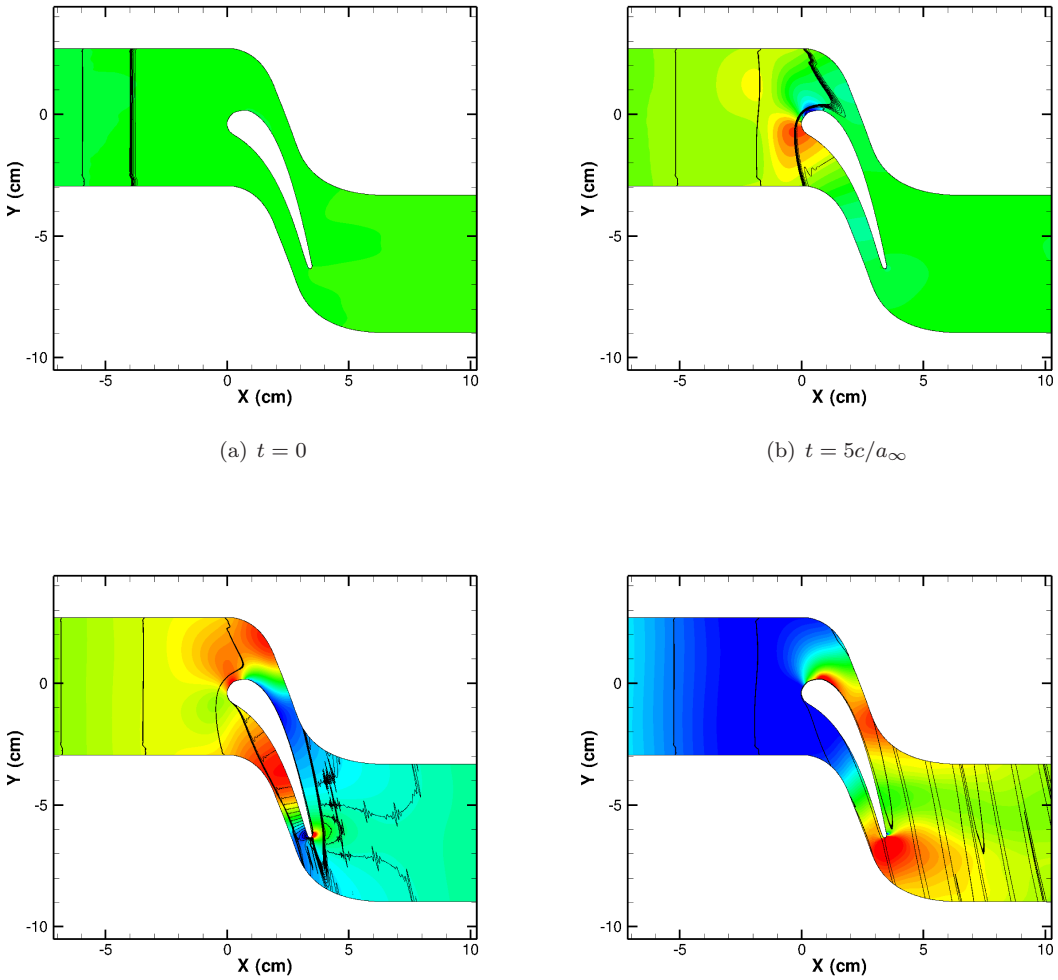

(a) $t = 0$

(b) $t = 5c/a_\infty$

(c) $t = 10c/a_\infty$

(d) $t = 15c/a_\infty$

Figure 4.12: Four consecutive instantaneous views of the density disturbance (solid lines) and pressure disturbance (contours) corresponding to plane wave of 1000 Hz. Time increases from left to right. Density contour lines of $|\rho'| \leq 1.0 \times 10^{-3}\rho_\infty$ and pressure contours of $|P'| \leq 1.0 \times 10^{-3}p_\infty$ are shown.

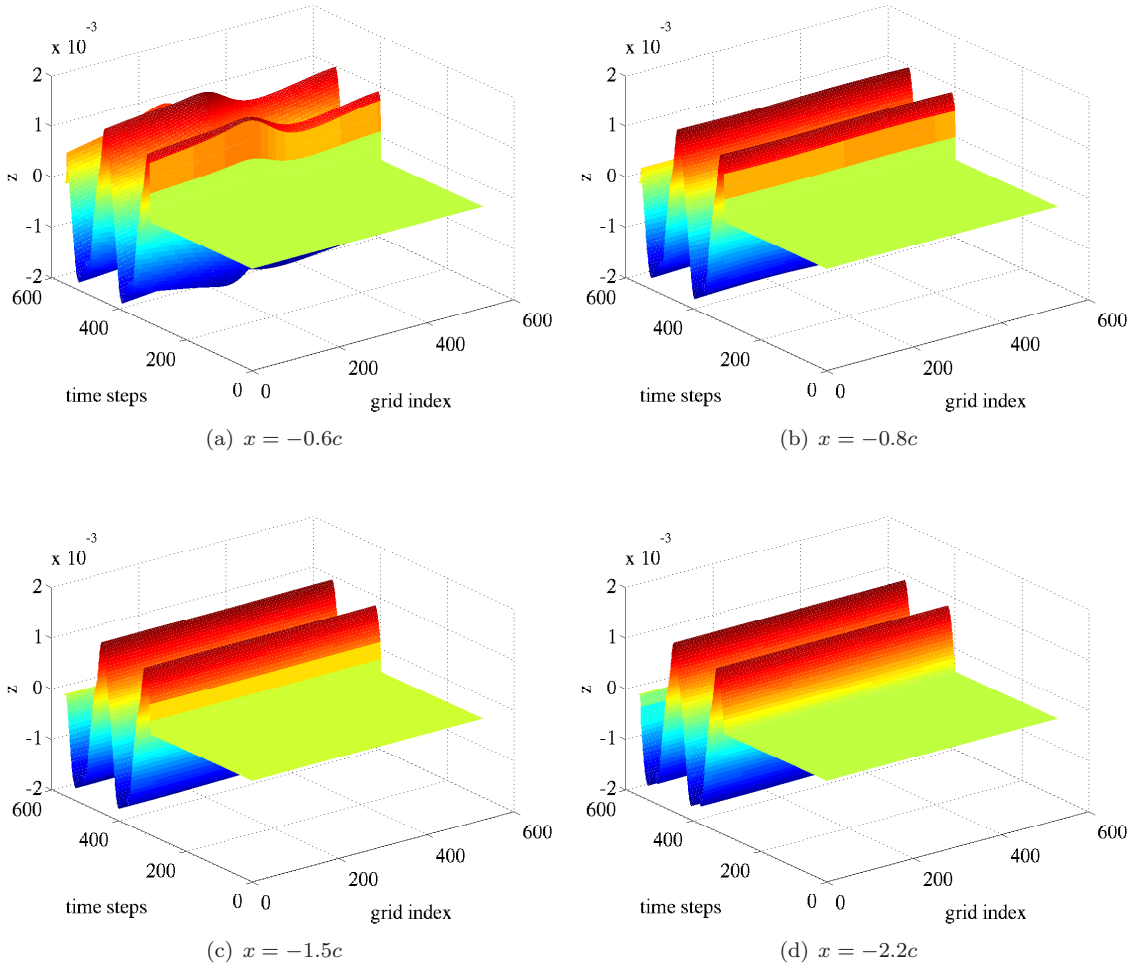

(a) $x = -0.6c$ (b) $x = -0.8c$

(c) $x = -1.5c$ (d) $x = -2.2c$

Figure 4.13: 3-dimensional representation of azimuthal and temporal variation of pressure fluctuations at various upstream probe stations. The z-label is$|p'/\gamma p|$

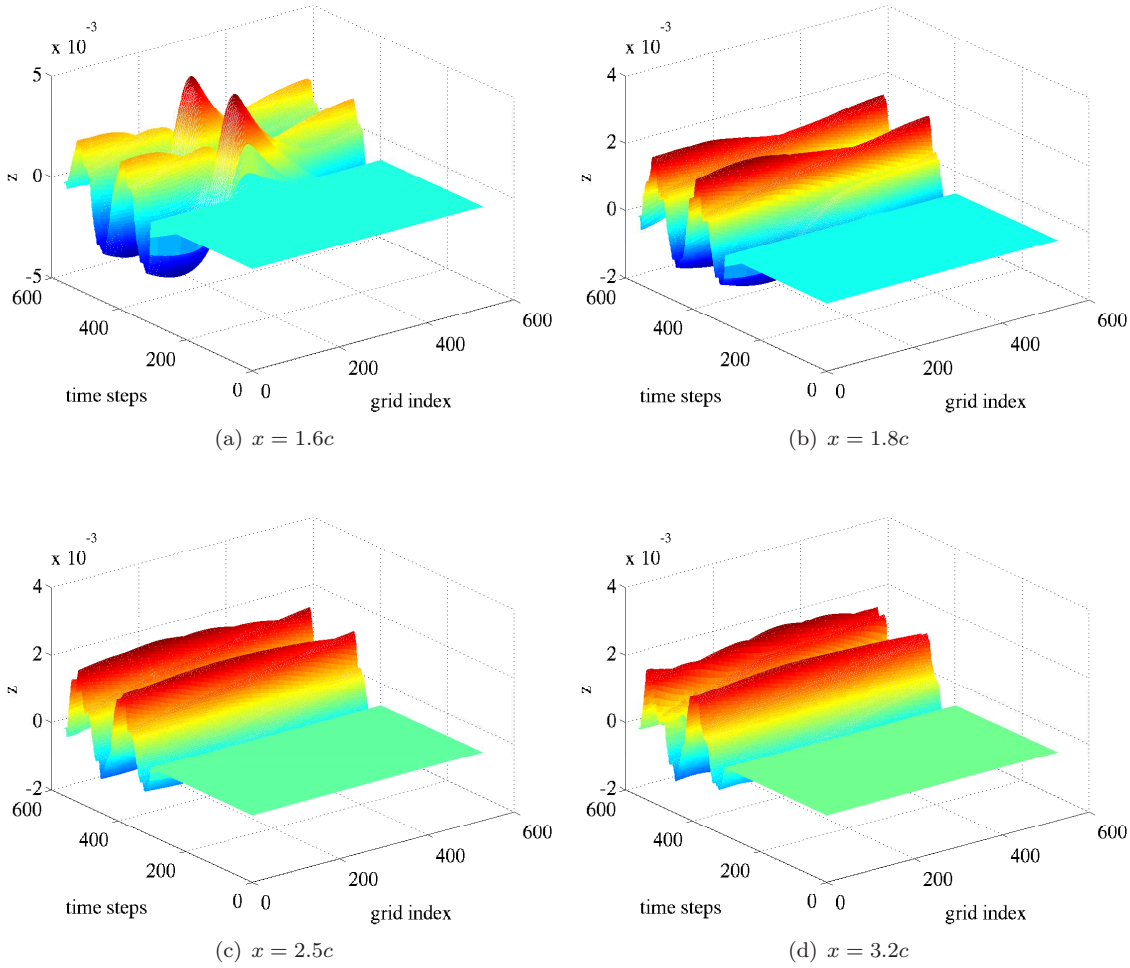

(a) $x = 1.6c$ (b) $x = 1.8c$

(c) $x = 2.5c$ (d) $x = 3.2c$

Figure 4.14: 3-dimensional representation of azimuthal and temporal variation of pressure fluctuations at various downstream probe stations. The z-label is$|p'/\gamma p|$

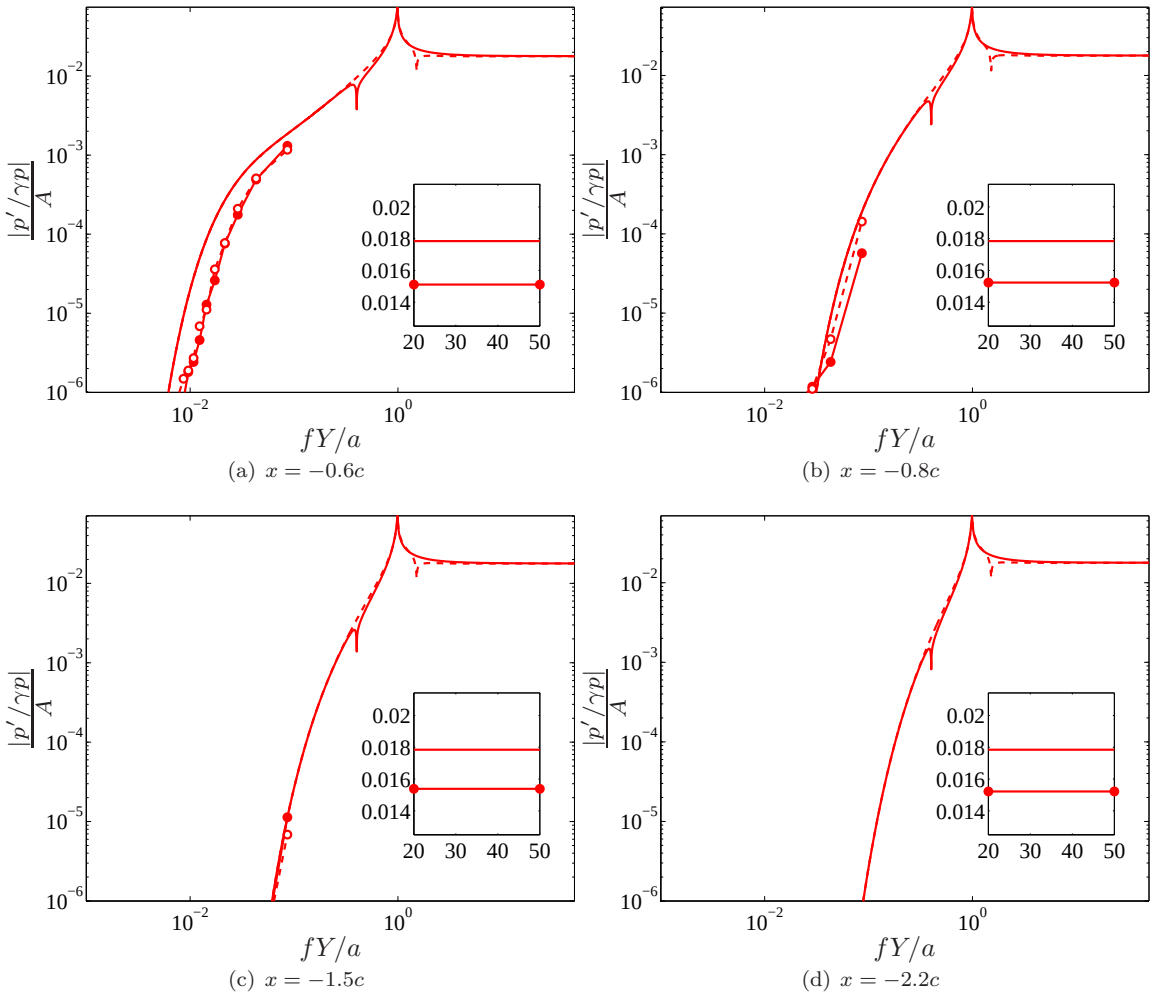

(a) $x = -0.6c$ (b) $x = -0.8c$

(c) $x = -1.5c$ (d) $x = -2.2c$

Figure 4.15: Comparison between pressure fluctuation magnitude of ADT and DNS results at the downstream probe stations. Legend: — ADT prediction for right moving wave; ● DNS result for right moving wave; – – – ADT prediction for left moving wave; ○ DNS result for left moving wave. Inset figures show the plane azimuthal mode corresponding to different cases.

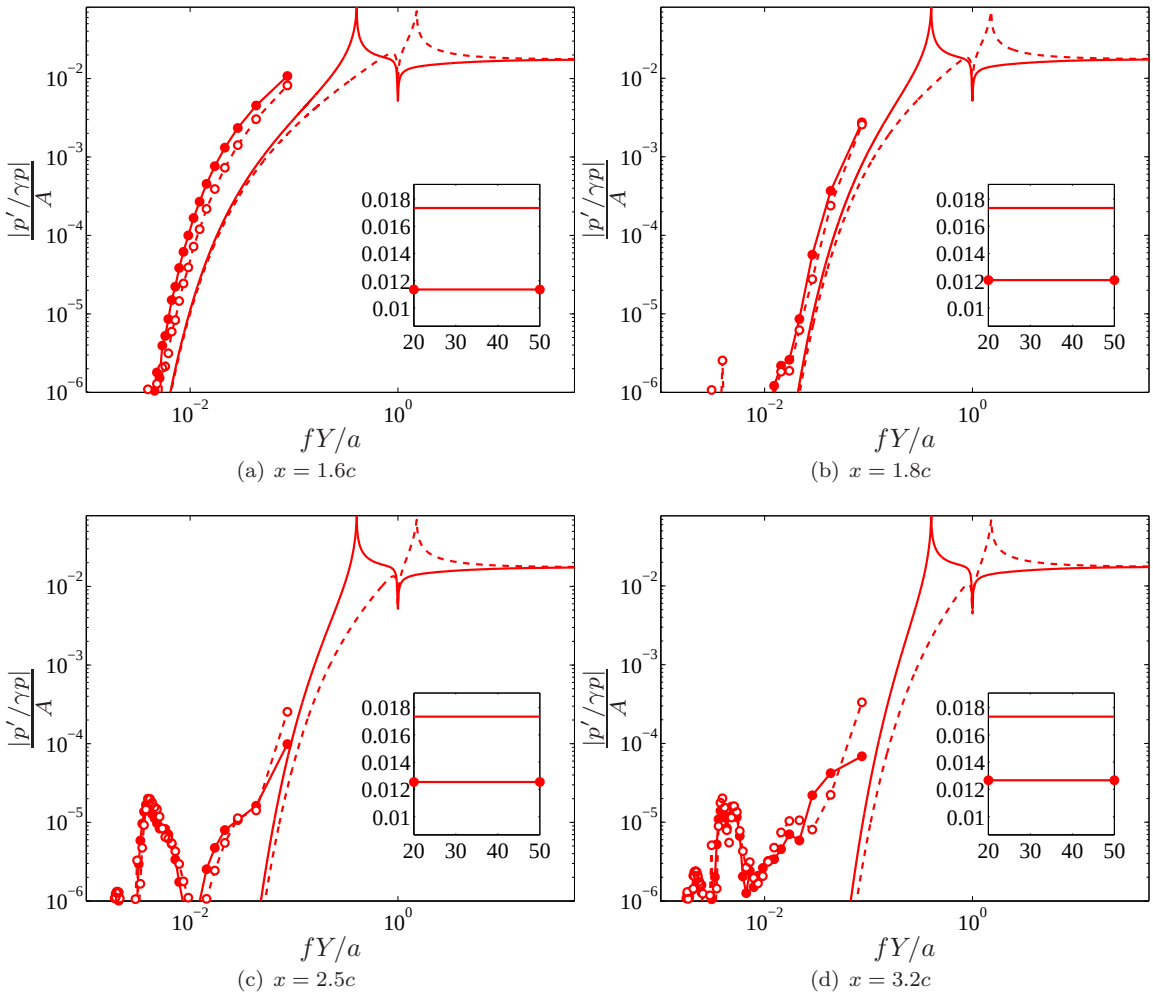

(a) $x = 1.6c$ (b) $x = 1.8c$

(c) $x = 2.5c$ (d) $x = 3.2c$

Figure 4.16: Comparison between pressure fluctuation magnitude of ADT and DNS results at the downstream probe stations. Legend: — ADT prediction for right moving wave; ● DNS result for right moving wave; – – – ADT prediction for left moving wave; ○ DNS result for left moving wave. Inset figures show the plane azimuthal mode corresponding to different cases.

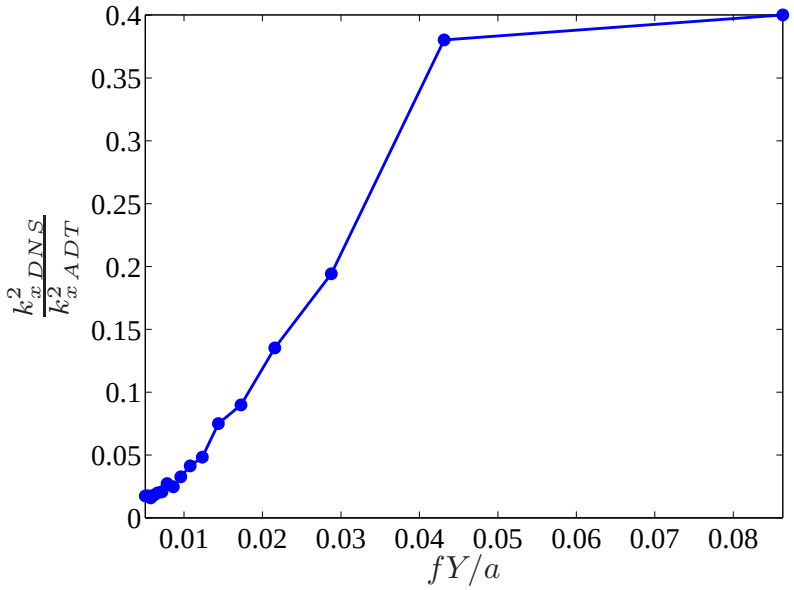

(a) Upstream

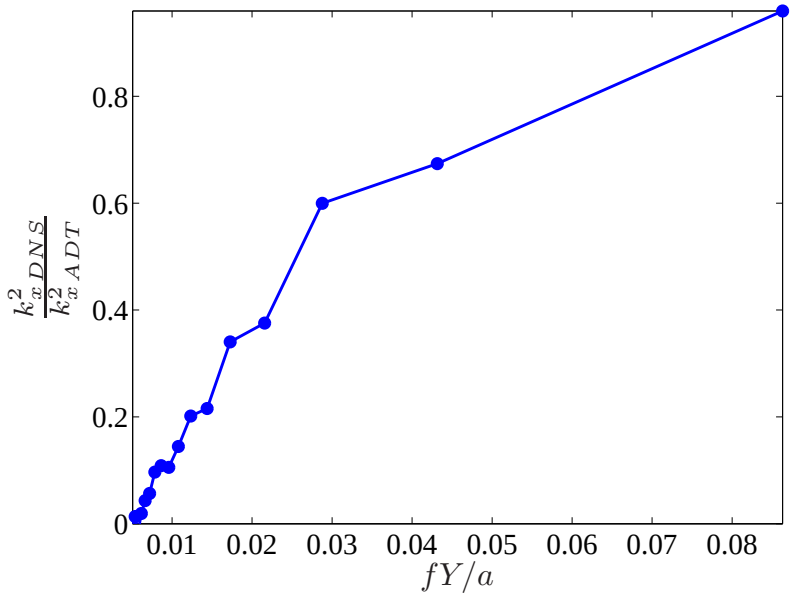

(b) Downstream

Figure 4.17: Comparison of axial decay rate between the DNS results and ADT predictions. Legend: ● right moving wave, 1000 Hz;

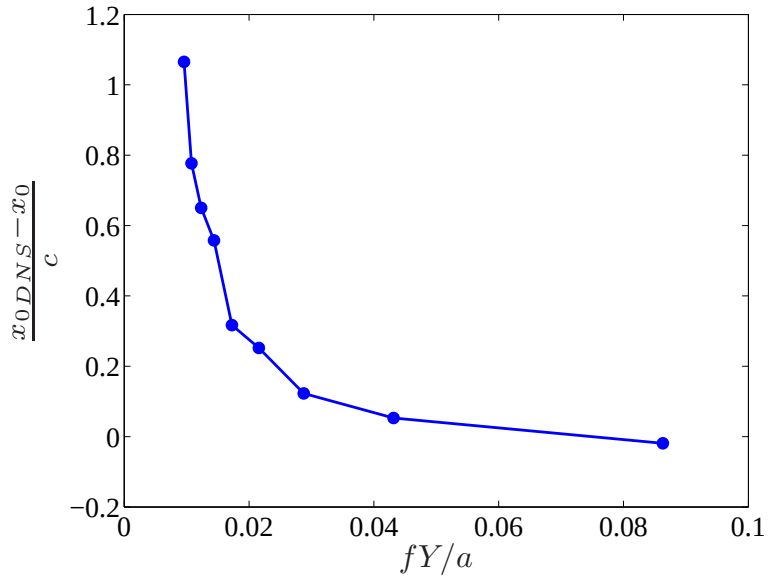

(a) Upstream

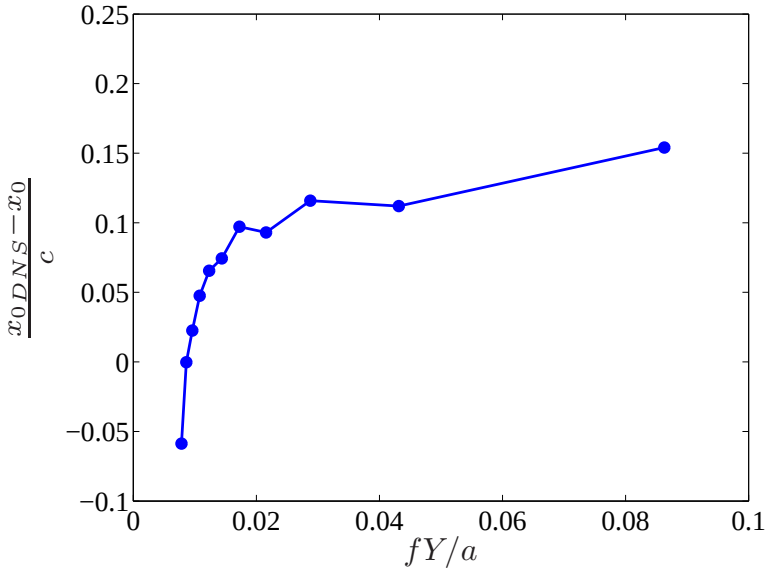

(b) Downstream

Figure 4.18: Location of perceived noise source in DNS results and its relative distance from leading and trailing edges for upstream and downstream waves. $x_0 = x_L E$ for upstream and $x_0 = x_T E$ for downstream. Legend: ● right moving wave, 1000 Hz;

Chapter 5

Conclusions and future work

5.1 Summary

The purpose of the above presented work was to carry out direct numerical simulations of the interaction of an entropy disturbance with a turbine blade row. These DNS results were then used to verify and evaluate the applicability of actuator disk theory. Two different sets of operating conditions were used to carry out direct numerical simulations corresponding to conditions of a 1980s era turbine and those of more modern turbines. Entropy disturbances introduced in the free stream inviscid flow were of the form of plane waves as well as high frequency, localized pulses. The actuator disk theory was implemented numerically and verified. The ADT predictions were obtained for the two different operating conditions mentioned above and were compared against the DNS results.

5.2 Conclusions

The interaction of an entropic disturbance with the linear cascade of downstream stator vane has been simulated in order to understand the indirect combustion noise. After attaining a sufficiently steady, grid-converged baseline mean flow, an entropic disturbance was added to the freestream. This entropic disturbance convected with the mean flow and flowed downstream. No pressure disturbance field was caused by this convection until it reached the leading edge of the stator vane. As entropy fluctuations passed over the leading edge, its acceleration due to stagnation points, the suction and pressure surfaces, and deflection due to wall boundary conditions led to pressure

fluctuations that, in turn, led to noise. The entropy disturbance went through extreme acceleration and deflection throughout its interaction with the blade and was stretched by the highly-nonuniform mean flow and created, among other things, local pockets of reduced momentum. These momentum deficits were accompanied by a non-uniform pressure field which had support over a larger region. When the pressure disturbance field associated with the entropy disturbance interacted with the blade's trailing edge, it was scattered into sound. Both upstream and downstream traveling pressure waves were generated and pressure fluctuations were propagated in the far field.

To understand actuator disk predictions, a comparison was made between the ADT and simulation results. These comparisons led to a better understanding of the results obtained as well as brought out some of the limitations of ADT while examining the validity of its assumptions. The two dimensional Fourier transform in azimuthal direction and time revealed many aspects of the spatial and temporal spectra of the resultant pressure disturbance field. Spatial spectra of low frequency waves showed that in the current computational domain all the permissible wavelengths, except the plane mode, were small enough to be cut-off which led to a complex-valued axial wavenumber and, hence, exponential decay with axial distance. Simulation results, in agreement with ADT predictions, show that the pressure fluctuation amplitudes corresponding to these wavelengths were exponentially decaying with the downstream and upstream distances. The amplitude of the pressure fluctuations corresponding to the planar cut-on mode were independent of the downstream or upstream distance from the blade because of its real-valued axial wavenumber. Unlike ADT, however, the planar mode pressure disturbance amplitudes obtained by DNS results are not independent of frequency. Further, the magnitude of the pressure fluctuation corresponding to planar mode deviated from ADT predictions by 20%.

The frequency dependent planar mode values led us to look closely at the ADT assumptions of negligible chord length as well as low pitch-chord ratio. The actuator disk theory ignores the details of the blade under the assumption that wavelengths of all the disturbances are much longer than the chord length of the blade and replaces it with a discontinuity at position x_0, referred in this thesis as the origin of the noise source. Actuator disk theory also only uses the inlet and outlet flow Mach number and flow angle to compute the pressure disturbance field caused by an input

entropy disturbance. It was observed that for a low-frequency input entropy wave the decay rates for modes of larger values of fY/a are very well predicted but as this parameter gets smaller, the matching between ADT predictions and simulation results worsened. The measured decay rate for smallest wavelengths was invariably lower than the ADT predictions. These observations show that ignoring blading details altogether is not entirely correct and, hence, ADT may not produce accurate predictions, especially at smaller wavelengths. The location of noise source had been computed using DNS results and it was found that ADT predictions are reasonable for low-frequency waves if we keep the leading edge of the blade as origin of noise source for upstream traveling waves whereas the trailing edge is better suited location for x_0 when it comes to downstream traveling waves.

It was observed that high-frequency localized pulses led to much higher diversions from ADT predictions, especially upstream of the blade. This happens because at higher frequencies, when axial wavelengths involved are comparable to the chord length of the blade, the assumption of ignoring blade details is no longer valid, including that the phase difference between the upstream and downstream waves is also non-negligible.

5.3 Future work

The work presented above had many limitations. First, the 2-D simulation model was limited in its ability to capture the 3-dimensional phenomenon in its entirety. Thus, a 3-dimensional simulation is needed to capture the effects of details of a blade on indirect combustion noise. Secondly, the computational domain chosen did not permit existence of higher non-planar wavelengths in azimuthal directions which limited our understanding of wavelengths which are cut-on. Thus, in the future studies it is advisable to use computational domains having a larger azimuthal space. Thirdly, it was observed that high frequency localized entropy pulse behaved differently than a plane wave entropic disturbance, so that a good topic to explore would be a modified ADT which included higher frequency disturbances.

References

[1] *Noise Sources*, Aeroacoustics of Flight Vehicles: Theory and Practice Vol.1, edited by H. H. Hubbard (Acoustical Society of America, Woodbury,NY, 1995); *Noise Control*, Aeroacoustics of Flight Vehicles: Theory and Practice Vol. 2, edited by H. H. Hubbard Acoustical Society of America, Woodbury, NY, 1995.

[2] W. C. Strahle, "A review of combustion generated noise," Progress in Astronautics and Aeronautics **37**, 229, (1975).

[3] N. A. Cumpsty and F. E. Marble, "Core noise from gas turbine exhausts," Journal of Sound and Vibration **54**, 297, (1977).

[4] R. N. Kumar, *Further experimental results on the structure and acoustics of turbulent jet flames,* In Aeroacoustics: Jet Noise, Combustion and Core Engine Noise, Progress in Astronautics and Aeronautics Vol. 43, edited by I. R. Schwartz, (AIAA, New York, 1976), pp. 483−507.

[5] K.K. Singh, S.H. Frankel, and J.P. Gore, "Study of spectral noise emissions from standard turbulent non-premixed flames," AIAA Journal, **42**, 931, (2004).

[6] K. Ramamurthi and R. K. Patnaik, "Noise reduction in non-premixed lifted-jet flames," Applied Scientific Research **72**, 49, (2004).

[7] M. Ihme, H. Pitsch, and D. J. Bodony, "Radiation of noise in turbulent non-premixed flames," Proceedings of the Combustion Institute **32**, 1545, (2009).

[8] R. Rajaram and T. Lieuwen, "Parametric studies of acoustic radiation from turbulent premixed flames," Combustion Science and Technology **175**, 2269, (2003).

[9] R. Rajaram and T. Lieuwen, "Effect of approach flow turbulence characteristics on sound generation from premixed flames," Presented at the 42nd AIAA Aerospace Sciences Meeting and Exhibit, Reno, NV, 2004, AIAA Paper No. 2004−0461.

[10] S. Bragg, "Combustion noise,", Journal of the Institute of Fuel **36**, 12 (1963).

[11] M. J. Lighthill, "On sound generated aerodynamically I. General theory,"Proceedings of the Royal Society A **211**, 564, (1952).

[12] W.C. Strahle, "On combustion generated noise", Journal Fluid Mechanics **49**, 399, (1971).

[13] D. G. Crighton, A. P. Dowling, J. E. Ffowcs Williams, M. Heckl, and F. G. Leppington. *Modern Methods in Analytical Acoustics.* Springer-Verlag, New York, 1996.

[14] M. S. Howe, "The generation of sound by aerodynamic sources in an inhomogeneous steady flow," Journal Fluid Mechanics **67**, 597, (1975).

[15] J. E. Ffowcs Williams and M. S. Howe, "The generation of sound by density inhomogeneities in low Mach number flows," Journal Fluid Mechanics **70**, 605, (1975).

[16] F. E. Marble and S. M. Candel, "Acoustic disturbance from gas nonuniformities convected through a nozzle," Journal of Sound and Vibration **55**, 225, (1977).

[17] N. A. Cumpsty, "Jet engine combustion noise: Pressure, entropy, and vorticity perturbations produced by unsteady combustion or heat addition," Journal of Sound and Vibration **66**, 527, (1979).

[18] Y. L. Sinai, "The generation of combustion noise by chemical inhomogeneities in steady, low-Mach-number flows," Journal Fluid Mechanics **99**, 383, (1980).

[19] F. Bake, N. Kings, A. Fischer, and I. Rohle, "Experimental investigation of the entropy noise mechanism in aero-engines," International Journal of Aeroacoustics **8**, 125, (2009).

[20] F. Bake, C. Richter, B. Muhulbauker, N. Kings, I. Rohle, F. Thielf, and B. Noll, "The entropy wave generator (EWG): a reference case on entropy noise" Journal of Sound and Vibration **326**, 574, (2009).

[21] J.E. Ffowcs Williams, D. L. Hawkings, "Sound generation by turbulence and surfaces in arbitrary motion," Philosophical Transactions of the Royal Society A **264**, 321, (1969).

[22] Cumpsty, N. A. and Marble, F. E., "The interaction of entropy fluctuations with turbine blade rows; a mechanism of turbojet engine noise," Proceedings of Royal Society London A, **357**, 323, (1977).

[23] M. Leyko, F. Nicoud, S. Moreau, and T. Poinsot, *Proceedings of the 2008 Summer Program Center for Turbulence Research,* Stanford University, Stanford, CA, 2008, pp. 343-354.

[24] F. Bake, N. Kings, and I. Rohle, "Fundamental mechanism of entropy noise in aero-engines: Experimental investigation," Journal of Engineering for Gas Turbines and Power **130**, 011202, (2008).

[25] M. S. Howe, "Indirect combustion noise," Journal Fluid Mechanics **569**, 267, (2010).

[26] M. Leyko, F. Nicoud, S. Moreau, and T. Poinsot, "Comparison of direct and indirect combustion noise mechanisms in a model combustor," AIAA Journal **46**, 2282, (2008).

[27] I. Duran, S. Moreau, "Analytical and numerical study of the entropy wave generator experiment on indirect combustion noise," Presented at the 17th AIAA/CEAS Aeroacoustics Conference, Portland,OR, 2011, AIAA Paper No. 2011-2829.

[28] C. K. W. Tam, N. N. Pastouchenko, J. Mendoza, and D. Brown, *Combustion noise of auxiliary power units,* Presented at the 11th AIAA/CEAS Aeroacoustics Conference, Monterey, CA, 2005, AIAA Paper No. 2005- 2829.

[29] Miles, J.H., "Separating turbofan engine noise sources using auto- and cross spectra from our microphones," AIAA Journal **46**, 61, (2008).

[30] N. Kings, K. Knolbloch, L. Enghardt, F. Bake, "Indirect combustion noise: experimental investigation of the vortex sound generation mechanism," Presented at the 17th AIAA/CEAS Aeroacoustics Conference, Portland,OR, 2011, AIAA Paper No. 2011-2827.

[31] Bodony, D.J., "Scattering of an entropy disturbance into sound by a symmetric thin body," Physics of Fluids **21**, 096101, (2009).

[32] Stabe, R.G., Whitney, W.J., and Moffit., T.P., "Performance of a High-Work Low Aspect Ratio Turbine Tested with a Realistic Inlet Radial Temperature Profile" NASA TM-83655, 1984.

[33] Dorney, D.J., Sondak, D.L., "Eeffects of tip clearance on hot streak migration in a high-subsonic single-stage turbine," Journal of Turbomachinery **122**, 613, (2000).

[34] Strand, B., " Summation by parts for finite difference approximations for d/dx," Journal of Computational Physics **110**, 47, (1994).

[35] Svard, M., Nordstrom, J., " A stable high-order finite difference scheme for the compressible Navier-Stokes equations: No-slip wall boundary conditions," Journal of Computational Physics **227** 4805, (2008).

[36] Svard, M., Carpenter, M.H., Nordstrom, J., " A stable high-order finite difference scheme for the compressible Navier-Stokes equations:far-field boundary conditions," Journal of Computational Physics **225** 1020, (2007).

[37] Bodony, D.J. , "Accuracy of the simultaneous-approximation-term boundary condition for time-dependent problem," Journal of Scientific Computing **43 (1)**, 118, (2010).

[38] Bodony, D.J. , "Analysis of sponge zones for computational fluid mechanics," Journal of Computational Physics **212**, 681, (2006).

[39] Sherer, S.E., Scot, J.N., "High-order compact finite-difference methods on general overset grids," Journal of Computational Physics **210**, 459, (2005).

[40] Sherer, S.E., Visbal, M.R., Galbraith, M.C., "Automated processing tools for use with a high-order overset-grid algorithm," AIAA Paper 2006-1147, 2006.

[41] Visbal, M.R., Gaitonde, D.V., "On the use of High-order Finite Difference Schemes on Curvilinear and Deforming Meshes," Journal of Computational Physics **181**, 155, (2002).